Reprinted from MONTHLY WEATHER REVIEW, Vol. 118, No. 2, February 1990
American Meteorological Society

Numerical Simulations of Cold Air Advection over the Appalachian Mountains and the Gulf Stream

CHING-YUANG HUANG AND SETHU RAMAN

Department of Marine, Earth and Atmospheric Sciences, North Carolina State University, Raleigh, North Carolina

(Manuscript received 13 March 1989, in final form 8 September 1989)

ABSTRACT

Cold air advection over the Gulf Stream off the Carolinas and the Appalachian Mountains is studied using idealized two-dimensional cases for the Genesis of Atlantic Lows Experiment (GALE) IOP 2 conditions. An anelastic hydrostatic mesoscale model is used. Turbulent transfer in the planetary boundary layer, diurnal heating, cloud dynamics, atmospheric longwave and shortwave radiation and subgrid cumulus parameterization are included in the model.

Model results show that the geometry of the oceanic and coastal rainbands depends on the direction of the ambient flow (onshore or offshore). For onshore flows, the rainbands remain in the vicinity of the oceanic baroclinic zone. The rainbands become transient and migrate downwind of the Gulf Stream front for offshore flows. Depths of the marine boundary layer (MBL) and the cloud (or rain) bands depend more on the ambient flow speed than its direction. The rainbands develop primarily in response to the strong low level convergence.

As expected, southward winds are produced at the eastern side of the Appalachian Mountains for onshore conditions. A significant amount of the turning, however, results from the baroclinic zone over the ocean. Upstream influence of the mountain intensifies the updrafts in the MBL and moves the oceanic rainbands further offshore. The effects of the atmospheric longwave and shortwave radiation, subgrid cloud heating and diurnal ground heating are of secondary importance in influencing the structure of the MBL as compared to the surface turbulent heat fluxes. Diurnal effects can change the coastal inland flow regime considerably, resulting in a local breeze and the formation of another cloud (or rain) band.

1. Introduction

Cold air masses advecting over the United States during the winter season often undergo significant changes when they encounter heterogeneous topography (e.g., Miller 1946; Locatelli et al. 1989). Offshore of the Carolinas, the warm (about 25°C) Gulf Stream is associated with surface temperature gradients in the coastal ocean and a large air–sea temperature difference (Wayland and Raman 1989). The intense land–air–sea interaction is believed to be responsible for the so-called Gulf Stream rainbands (Hobbs 1987; Sienkiewicz et al. 1989). In addition, the Appalachian Mountains, roughly parallel to the coastline over the Carolinas, appear to play a role in the generation of mesoscale weather events. One such event is the cold air damming when a continental high pressure system develops near the northeastern coast of the United States. The Genesis of Atlantic Lows Experiment (GALE) (Dirks et al. 1988) has provided a good opportunity to investigate the effects of the Appalachian Mountains and the Gulf Stream on the East Coast winter storms.

Corresponding author address: Dr. Sethu Raman, Department of Marine, Earth and Atmospheric Sciences, Box 8208, Raleigh, NC 27695.

Numerical studies on the modification of the atmospheric boundary layer by air–sea interaction have been conducted by many investigators (e.g., Brost 1976; Moeng and Arakawa 1980; Atlas et al. 1983; Wai and Stage 1989). In the simulations of the marine boundary layer (MBL) induced by a single (Gulf Stream) front, Wai and Stage (1989) showed that a convective PBL forms offshore and slopes up seawards in response to the increasing modification of the low level air. The earlier stages of the development of mesoscale circulation induced by the steady ocean warming are not significantly different from those obtained in sea breeze simulations (e.g., Mahrer and Pielke 1977, 1978). The low level constant heating-induced circulation, however, will greatly differ from the diurnal sea breeze during the later stages of the development. There is no steady state linear solution for such a problem if the net heating in the flow cannot be efficiently diffused out by the physical cooling processes (Smith and Lin 1982). Huang and Raman (1988) found that for offshore flow the speed of the circulation front downwind of the Gulf Stream depends primarily on the ambient flow speed. Changing the initial upper level moisture above the MBL did not have much influence on the circulation.

In this study, numerical experiments for onshore flows are conducted to investigate the conditions con-

ducive for the generation of the oceanic rainbands and the role of the Appalachian Mountains in causing them. The GALE inner region chosen for simulations in this study is the same as in Fig. 1 of Dirks et al. (1988). A primary ridge of the Appalachian Mountains lies near the western edge of the domain parallel to the coastline and the Gulf Stream. Distances to the coastline and the western edge of the Gulf Stream from the Appalachians are about 400 and 550 km, respectively. This topography is particularly favorable for two-dimensional (2-D) model simulations if the model horizontal axis is chosen to be normal to the coastline with the model domain oriented northwest to southeast.

A three-dimensional (3-D) mesoscale model could provide a better dynamical understanding. It is expensive, however, because of the very large numerical domain required to reduce the influence of the lateral boundary conditions caused by the elongated shape of the Appalachian Mountains. Two-dimensional simulations for the effects of this particular geometry of the topography allow us to reduce the computer cost considerably and avoid the boundary-value problem, but the two dimensionality of the flow will differ from the results of the 3-D simulations. Mountain upstream influence is one of the behaviors that will be different when a two-dimensionality of the flow is assumed as discussed by Pierrehumbert and Wyman (1985) and Smolarkiewicz et al. (1988). In a 2-D stratified hydrostatic flow, the upstream influence extends far upstream (Pierrehumbert and Wyman 1985). For the 3-D flow, the influence is essentially limited near an isolated obstacle (Smith 1979; Smolarkiewicz et al. 1988).

The diurnal change in the ground temperature is important for the flow regime over land, especially near the mountains. For the mountain flow, the destabilization of a PBL caused by ground heating could significantly change its dynamical controlling parameter, the Froude number $\mathrm{Fr} = U/Nh$, where U is the mean upstream wind speed, h the characteristic height of the mountain and N the atmospheric Brunt–Väisälä frequency. For the coastal flow, surface heating could produce a localized circulation due to the sea breeze effect. This circulation in turn may influence the adjacent MBL. Ground heating thus needs to be specified to simulate land–air–sea interaction processes properly.

The 2-D model used to study the problem is an anelastic hydrostatic mesoscale model with a PBL turbulence closure based on the turbulent kinetic energy equation. A surface energy budget equation is used for ground temperature. To include the effects of subgrid cumuli that cannot be explicitly resolved by our grid mesh (with a horizontal resolution of 10 km), a variation of the Kuo-type cumulus parameterization scheme is used. In addition, atmospheric shortwave and longwave radiation is incorporated in the model.

A brief description of the physical components of the numerical model including the PBL turbulent transfer, atmospheric radiation, surface energy budget and the subgrid cumulus parameterization is given in section 2. Numerical schemes and the initial and boundary conditions used in the model are described in section 3. Results from the numerical experiments that pertain to the structure of the MBL, the geometry of the oceanic rainbands, cold air damming and the role of the Appalachian Mountains are discussed in section 4.

2. The model

The numerical model presented in this paper is an improved version of the one given by Huang and Raman (1988, hereafter referred to as HR). Most of the model components and the numerical schemes are presented elsewhere (Huang 1989); hence details of the model will be omitted here for brevity.

a. Model equations

Governing equations of the basic flow expressed in the terrain-following coordinate σ are as follows:

$$\frac{\partial u}{\partial t} = -u\frac{\partial u}{\partial x} - \tilde{w}\frac{\partial u}{\partial \sigma} + fv - \theta_v\frac{\partial \pi}{\partial x} - g(1-\sigma)\frac{\partial \hat{E}}{\partial x} + \frac{\partial}{\partial x}\left(K_H\frac{\partial u}{\partial x}\right) + \frac{1}{H-\hat{E}}\frac{\partial}{\partial \sigma}(\overline{-u'w'}), \quad (1)$$

$$\frac{\partial v}{\partial t} = -u\frac{\partial v}{\partial x} - \tilde{w}\frac{\partial v}{\partial \sigma} - fu + fU_g + \frac{\partial}{\partial x}\left(K_H\frac{\partial v}{\partial x}\right) + \frac{1}{H-\hat{E}}\frac{\partial}{\partial \sigma}(\overline{-v'w'}), \quad (2)$$

$$\frac{\partial \theta}{\partial t} = -u\frac{\partial \theta}{\partial x} - \tilde{w}\frac{\partial \theta}{\partial \sigma} + \frac{\partial}{\partial x}\left(K_H\frac{\partial \theta}{\partial x}\right) + \frac{1}{H-\hat{E}}\frac{\partial}{\partial \sigma} \times (\overline{-w'\theta'}) + Q_{\mathrm{CON}} + Q_{\mathrm{CL}} - Q_{\mathrm{EV}} + Q_{\mathrm{RAD}}. \quad (3)$$

$$\frac{\partial q}{\partial t} = -u\frac{\partial q}{\partial x} - \tilde{w}\frac{\partial q}{\partial \sigma} + \frac{\partial}{\partial x}\left(K_H\frac{\partial q}{\partial x}\right) + \frac{1}{H-\hat{E}}\frac{\partial}{\partial \sigma} \times (\overline{-w'q'}) - M_{\mathrm{CON}} + M_{\mathrm{EV}} + M_{\mathrm{CL}}. \quad (4)$$

$$\frac{\partial q_l}{\partial t} = -u\frac{\partial q_l}{\partial x} - \tilde{w}\frac{\partial q_l}{\partial \sigma} + \frac{\partial}{\partial x}\left(K_H\frac{\partial q_l}{\partial x}\right) + \frac{1}{H-\hat{E}}\frac{\partial}{\partial \sigma}(\overline{-w'q_l'}) + \frac{1}{\rho(H-\hat{E})}\frac{\partial \rho V_T q_l}{\partial \sigma} + M_{\mathrm{CON}} - M_{\mathrm{EV}}. \quad (5)$$

$$\frac{\partial \pi}{\partial \sigma} = -\frac{g(H-\hat{E})}{\theta_v}. \quad (6)$$

$$\frac{\partial \rho u(H-\hat{E})}{\partial x} + \frac{\partial \rho \tilde{w}(H-\hat{E})}{\partial \sigma} = 0 \quad (7)$$

where the terrain following coordinate is defined by

$$\sigma = \frac{z-\hat{E}}{H-\hat{E}} \quad (8)$$

with the model maximum height H and the terrain height $\hat{E}$. Equations (1) and (2) are momentum equations for wind components u in the x direction and v in the y direction, respectively, (3) is the thermodynamic equation for potential termperature θ, (4) and (5) are conservation equations for water vapor q and liquid water q_l, respectively, (6) is the hydrostatic equation and (7) the anelastic continuity equation. In the prognostic equations (1) to (4), terms involving K_H are for horizontal diffusion and terms with primed variables are for subgrid turbulence flux divergence. Note that in (2) U_g is the geostrophic wind component in the x direction. In this study, the positive-x axis points to the southeast and the positive-y axis to the northeast. The scaled pressure π from the Exner function is defined as

$$\pi = C_p\left(\frac{p}{p_{00}}\right)^{\kappa}, \kappa = \frac{R}{C_p} \tag{9}$$

where p is pressure with the reference pressure p_{00} set to 1000 mb. The virtual potential temperature, θ_v, is defined as

$$\theta_v = \theta(1 + 0.61q - q_l). \tag{10}$$

Here, the vertical velocity in the σ-coordinate, $\tilde{w}$, can be related to the vertical velocity in z-coordinate, w, by

$$w = \tilde{w}(H - \hat{E}) - (\sigma - 1)u\frac{\partial \hat{E}}{\partial x}. \tag{11}$$

The sink or source terms in Eqs. (3), (4) and (5) are described below as

Q_{CON} release rate of latent heat by condensed water vapor,
Q_{CL} release rate of latent heat by subgrid scale cloud due to condensation of water vapor,
Q_{EV} release rate of latent heat by evaporation of liquid water,
Q_{RAD} radiational cooling or heating,
M_{CON} condensation of water vapor,
M_{CL} moisture contribution due to the condensation of water vapor at subgrid scale, and
M_{EV} moisture contribution from the evaporation of liquid water.

Expressions for Q_{CON} and M_{CON} are given in HR. Following Brown (1974), the evaporation of liquid water, Q_{EV}, is taken as

$$Q_{EV} = \frac{L_c}{\pi} M_{EV} \tag{12}$$

where L_c is the latent heat of condensation and

$$M_{EV} = \delta_e 0.0045\rho^{-0.325} q_l^{0.675}(q_s - q) \tag{13}$$

with

$$\delta_e = \begin{cases} 1, & \text{if } q \leqslant q_s \\ 0, & \text{otherwise} \end{cases} \tag{14}$$

where q_s is saturation moisture. Terminal velocity for the liquid water, V_T, is assumed to be (Cotton 1976)

$$V_T = \begin{cases} 31.2(\rho q_l)^{0.125}, & T > 0°\text{C} \\ 5.9(\rho q_l)^{0.11}, & T \leqslant 0°\text{C} \end{cases} \tag{15}$$

where T is air temperature in °C and ρ air density in g cm^{-3}. A value of 1 g kg^{-1} is allowed for maximum content of liquid water q_l^* in the cloud.

b. Turbulent transfer

The similarity relationships given by Businger et al. (1971) are used for the surface layer in this study (for details see HR). For the outer layer of the PBL, a closure scheme based on the prognostic turbulent kinetic energy (TKE) equation is used. The TKE closure scheme is essentially that of Deardorff (1980). The vertical grid interval Δz is used in the boundary layer closures in our mesoscale model following Sun and Hsu (1988). The TKE closure used in this paper was found to be satisfactory based on the simulations of an idealized mesoscale flow over complex terrain (Huang and Raman 1989).

The vertical gradient of TKE is assumed to vanish at the upper boundary. The TKE equation was integrated for one hour with an initial boundary value of $3.75u_*^2$ at the surface to initialize the TKE field.

c. Surface energy balance

The land surface temperature is obtained from the surface energy balance equation

$$Q_G - \rho_0 C_p u_* \theta_* - \rho_0 L_c u_* q_* - R_S - R_L = 0 \tag{16}$$

where R_S is the net shortwave radiation and R_L the net longwave radiation on the ground and the first term, soil heat flux into the ground Q_G is defined as

$$Q_G = \rho_s c_s k_s \left.\frac{\partial T}{\partial z}\right|_G. \tag{17}$$

Here, T is the soil temperature, subscript G denotes the ground level, u_* surface layer friction velocity, θ_* flux temperature, q_* flux moisture, ρ_0 surface layer air density, ρ_s soil density, c_s specific heat capacity of soil and k_s the thermal diffusivity of soil. The determination of R_S follows Paltrige and Platt (1976) and Kasten and Czeplak (1980). For longwave radiation, the emissivities for the ground surface ϵ_g and the atmosphere ϵ_a are assumed to be unity in this study.

The temperature gradient of the soil layer can be specified as a function of the net radiation (e.g., Dear-

dorff 1978) or obtained by solving the soil heat conduction equation (referred to as method II)

$$\frac{\partial T}{\partial t} = \frac{\partial}{\partial z} k_s \frac{\partial T}{\partial z}. \tag{18}$$

Ten layers with a stretched grid mesh and an implicit numerical scheme are chosen to solve this equation. As proposed by Mahrer and Pielke (1977), the Newton–Raphson iterative method is efficient in obtaining the land surface temperature with the requirement that the residue in Eq. (16) is very small and the change in θ_* is negligible. Unfortunately, this method is time-consuming (McCumber and Pielke 1981). An alternative is to use a simplified form (referred to as method I) given by Deardorff (1978) as

$$\frac{\partial T_s}{\partial t} = \frac{2\sqrt{\pi}\, Q_G}{\rho_s c_s d_s} - \frac{2\pi}{\tau_s}(T_s - \bar{T}_d) \tag{19}$$

where T_s is the soil surface temperature and τ_s the time scale of diurnal cycle set to one day, $\bar{T}_d$ the mean deep soil temperature of the previous day, and d_s the penetrative depth of diurnal ground temperature into the underlying soil layer. This depth is estimated as $(k_s\tau_s)^{1/2}$ by Carlson et al. (1981). In this study, both $\bar{T}_d$ and T_s are assumed to be equal to the surface temperature at the final stage of mountain growth.

d. Radiative transfer

Scheme for the atmospheric radiative transfer is similar to the one adopted by Mahrer and Pielke (1977). This scheme takes into account the absorption of softwave energy by water vapor and the longwave radiation emitted by water vapor and carbon dioxide. The technique (Sasamori 1972) for radiative transfer formulation assumes an isothermal atmosphere and has been used to simplify the computing procedure.

e. Subgrid cloud parameterizations

To account for the subgrid cloud effects, a variation of Kuo's cumulus parameterization scheme (Kuo 1965, 1974; Anthes 1977) is used in this study. Only the subgrid scale deep clouds are considered; the subgrid scheme does not deal with shallow clouds. The cloud base σ_B is determined by the lifting condensation level (LCL) of each air parcel. Using the equilibrium temperature level (ETL) where the cloud temperature is the same as that of the environment, the cloud top σ_T is determined as the height below which there is no net heating (Pielke 1984). Thus, cloud overshooting can occur above the ETL. A maximum depth of 2 km is allowed for the cloud overshooting. The subgrid cloud effects are ignored if the active cloud depth (i.e., the depth between LCL and ETL) is less than 3 km. Details of the scheme are given in Huang (1989).

3. The numerical methods

To better resolve the effects of the Appalachian Mountains, the quadratic upstream scheme (Leonard 1979), which preserves phase and magnitude much better than the original Crowley scheme (1968), is used for the advection in this study. Our tests indicate this scheme to be comparable to the cubic upstream spline and the fourth-order leapfrog scheme. Vertical diffusion terms for the subgrid scale fluxes are represented by an implicit scheme in which a tridiagonal matrix is solved (Mahrer and Pielke 1978; Huang and Raman 1988).

For lateral boundary conditions of the prognostic variables in the model, the Orlanski's radiation condition (Orlanski 1976) with a forward-upstream scheme (Miller and Thorpe 1981) is applied to the inflow boundary grids (flow enters the numerical domain). The prediction equations are used at the outflow boundary grids (flow moves out of the numerical domain). Large scale forcing represented by initial pressure gradients is kept constant at the lateral boundaries.

At the lower boundary, the no slip condition is imposed. The sea surface temperature is specified and fixed after the adjustment period (the first integration hour in this study). The land surface temperature is computed using the surface energy budget equation. The relative humidity near the surface (for both land and ocean) is held constant. Pressure at the upper boundary is specified by the radiation boundary condition (Klemp and Durran 1983) since zero gradient conditions could cause a total wave reflection from the upper boundary (Klemp and Lilly 1978).

A low-pass linear filter (Shapiro 1971) is adopted in this study as in HR to remove waves of two horizontal grid intervals. This filter has little effect on the numerical solution of significant mountain waves (Durran and Klemp 1983). To obtain the initial conditions, the same procedure as in HR is adopted, which consists of solving the Ekman-gradient equation along with the TKE equation.

4. The results

Nine runs including some sensitivity tests were conducted in this study. Table 1 gives the descriptions of the numerical experiments. All simulations use a time interval of 60 s, 120 grids in the horizontal with a uniform grid size of 10 km and 20 stretched grids in the vertical. The solar angle corresponds to a day of IOP 2 of GALE (Dirks et al. 1988) in which several weather events including a coastal front, offshore cyclogenesis and a cold air outbreak occurred. The Appalachian Mountains are idealized by a bell-shaped Gaussian mountain with a maximum height of 2 km over grid 20 and a half-width of about 30 km. The sea surface temperature (SST) distribution is similar to the one in HR and is shown in Fig. 1 in which three temperature

TABLE 1. Descriptions of the two-dimensional numerical experiments for barotropic onshore and offshore flows over the GALE inner region.

Case	Subgrid cloud	Diurnal change*	Geostrophic wind	Notes for other model features
			Onshore flow ($m\ s^{-1}$)	
CD1	Off	Method I	$U_g = -10$, $V_g = 0.1$	RH = 80% within 3 km, then linearly decays to zero at 10 km; longwave and shortwave radiation
CD2	On	Method I	$U_g = -10$, $V_g = 0.1$	Same as case CD1
CD3	Off	Method II	$U_g = -10$, $V_g = 0.1$	Same as case CD1 but longwave radiation only
CD4	Off	Off	$U_g = -10$, $V_g = 0.1$	Same as case CD3
CD5	Off	Method II	$U_g = -10$, $V_g = 0.1$	Same as case CD3 except with the removal of Appalachian Mt.
CD6	Off	Method I	$U_g = -2.5$, $V_g = 0.1$	Same as case CD1
CD7	On	Method I	$U_g = -2.5$, $V_g = 0.1$	Same as case CD1
			Offshore flow ($m\ s^{-1}$)	
CA1	Off	Method I	$U_g = 10$, $V_g = 0.1$	Same as case CD1
CA2	Off	Method I	$U_g = 2.5$, $V_g = 0.1$	Same as case CD1

* Method I: Use of Eq. (19) in the text. Method II: Use of Eq. (18) in the text.

jumps indicate the coastal, midshelf and Gulf Stream temperatures, respectively. The soil layer is situated between grids 1 and 59 with an initial ground temperature of 3°C in contrast to the Gulf Stream value of 25°C starting from grid 75. The air–sea temperature difference has a maximum value of 22°C over the Gulf Stream. The imposed initial surface temperature gradient is quite large (but realistic), thus introducing a strong baroclinic PBL, as one would expect. As can be seen in Fig. 1, the observed small decrease in the SST (Wayland and Raman 1989) east of the Gulf Stream has been neglected. The assumption of constant SST in the Gulf Stream simplifies the influence of lateral boundary conditions without sacrificing the mesoscale structure of the atmosphere in the vicinity of the western edge of the Gulf Stream. Initial conditions for the moisture and liquid water are the same in all cases.

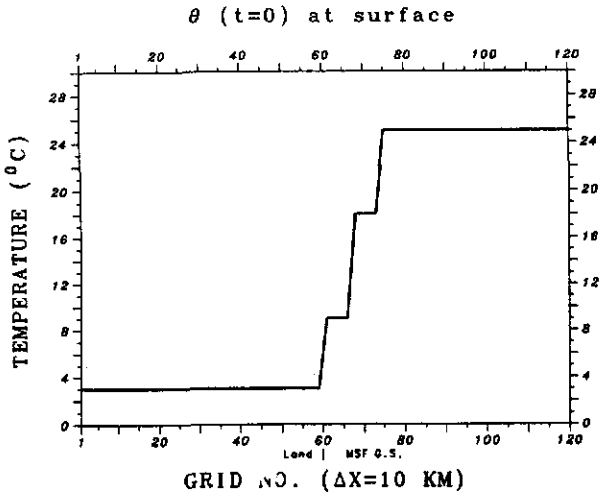

FIG. 1. Surface temperature distribution for the numerical experiment. The uniform ground temperature is 3°C (in grids 1 to 59). Three temperature jumps (from left to right) are associated with the coastline in grid 60, the midshelf front (MSF) in grid 68 and the western edge of the Gulf Stream (G.S.) in grid 75, respectively.

The model was integrated from 0500 LST (0 model hours) to 2100 LST (16 model hours). Initially, the lowest air is uniformly cold (3°C). The first hour (from 0500 to 0600 LST) is used for the mountain growth and the ocean warming. It is difficult to relate the model LST to the real time of the day because of the nonstationarity of the flow over the oceanic baroclinic zone. Therefore, diurnal heating is imposed in the model only to study the heating and moistening efficiency by the two different surfaces, ocean and land. Since the model time phase cannot be matched with real time, model initialization is only for a typical atmospheric situation. Onshore flow in the model typifies the advection from a high pressure system to the northeast and the offshore flow from a low pressure to the northwest of the GALE inner region.

a. Structure of the PBL for onshore and offshore flows

One would expect the strong baroclinic zone near the coast to modify the dynamics and thermodynamics of the flows. The thermodynamic structure can indicate the degree of air mass modification and provide an understanding of the processes involved.

The strong onshore flow is represented by a geostrophic wind of $U_g = -10\ m\ s^{-1}$ and $V_g = 0.1\ m\ s^{-1}$ in this study. The small but nonzero geostrophic wind component V_g is used in order to be consistent with the one in HR. For onshore flow, a slightly southerly wind component would indicate the presence of cold air damming over land. Figure 2 shows the potential temperature (θ) at different simulation hours for the strong onshore flow case CD1 (Table 1) without subgrid clouds. Model hours are indicated in the title of each figure. As can be seen from Fig. 2, a highly

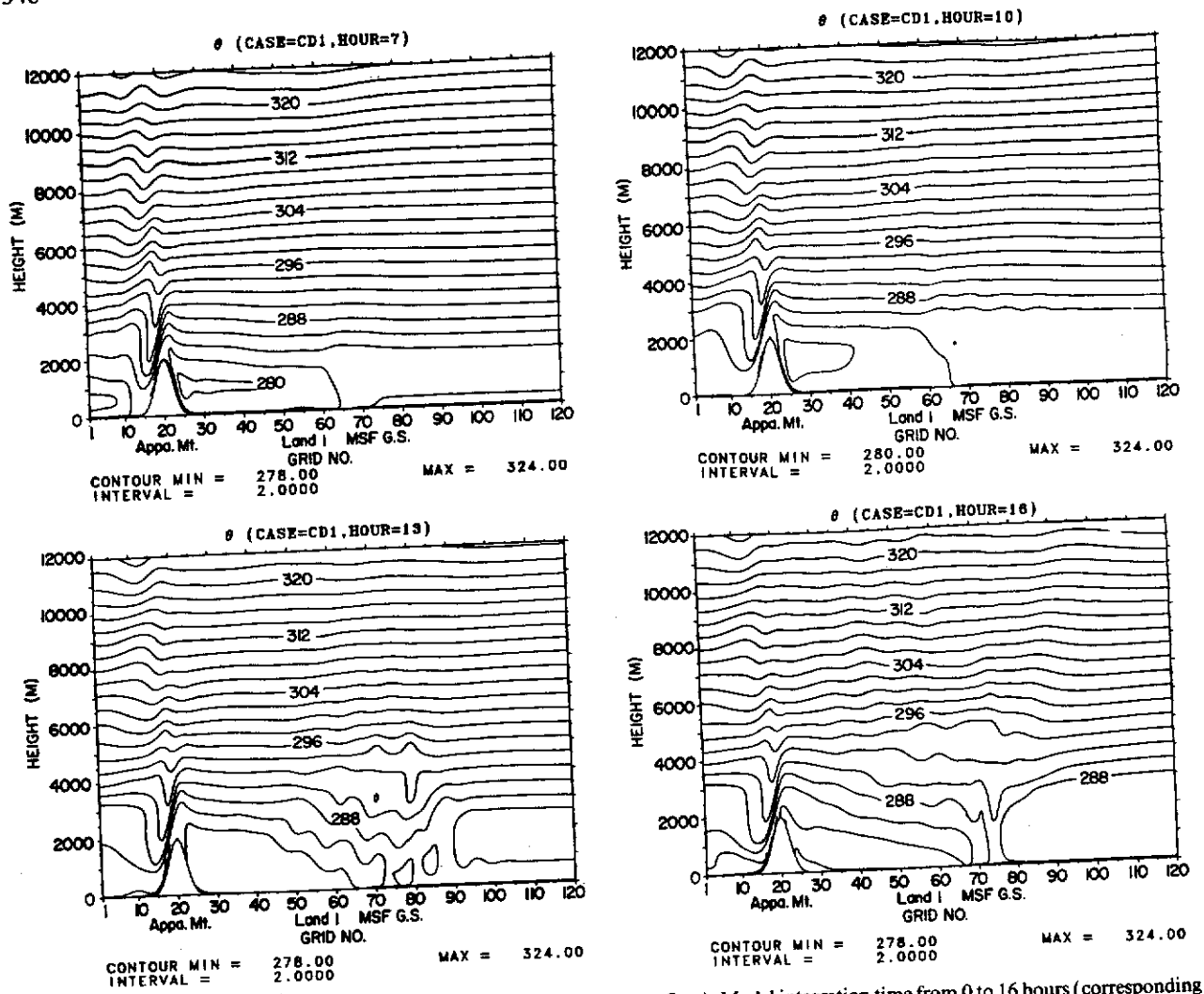

FIG. 2. Potential temperature fields for case CD1 (with the strong onshore flow). Model integration time from 0 to 16 hours (corresponding to 0500 to 2100 LST) is indicated above each figure. Contour unit is °K. Description of the cases are given in Table 1. Plotted symbols at the bottom of each panel are the same with those in Fig. 1 with the addition: "Appa. Mt." for the Appalachian Mountains.

convective MBL is fully developed for the strong onshore flow by 1800 LST (model hour 13). The height of the MBL can be clearly identified by the vertical profile of the potential temperature in the well-mixed CBl even before 1500 LST (model hour 10).

The thermodynamic structure shows strong development of the MBL in the vicinity of the Gulf Stream. The apparent development of the updrafts (between grids 70 and 85 in Fig. 14) after 1500 LST is in response to the increasing upper level moistening and destabilization. Before the cloud development, there is uniform thermal structure upwind of the western edge of the Gulf Stream, caused by the constant surface heating (uniform SST) to the east. This layer of neutral MBL is then destroyed by the development of the clouds over the baroclinic zone (grid number 70) to the west (see Fig. 12). Once the convective low-level structure has built up, the associated updrafts penetrate increasingly upward to reach the LCL. This results in the release of latent heat through condensation, which in turn intensifies the updrafts as will be shown in a later section (Fig. 14). For the flow regime over land, this feature of clouds in the PBL development is not present because of a relatively dry environment. By 2100 LST (model hour 16), the convective boundary layer (CBL) over land has been completely suppressed by the effects of nocturnal cooling as can be seen from the increased (stable) vertical gradient of the potential temperature. Over the ocean the MBL continuously develops and reaches a maximum height of 3 km to the east of the Gulf Stream frontal zone.

Figure 3 shows the potential temperature field for case CD6 with a weaker onshore flow (geostrophic wind $U_g = -2.5$ m s^{-1} and $V_g = 0.1$ m s^{-1}). A symmetric thermal structure begins to develop near the coastline at low levels around 1500 LST (model hour 10). This

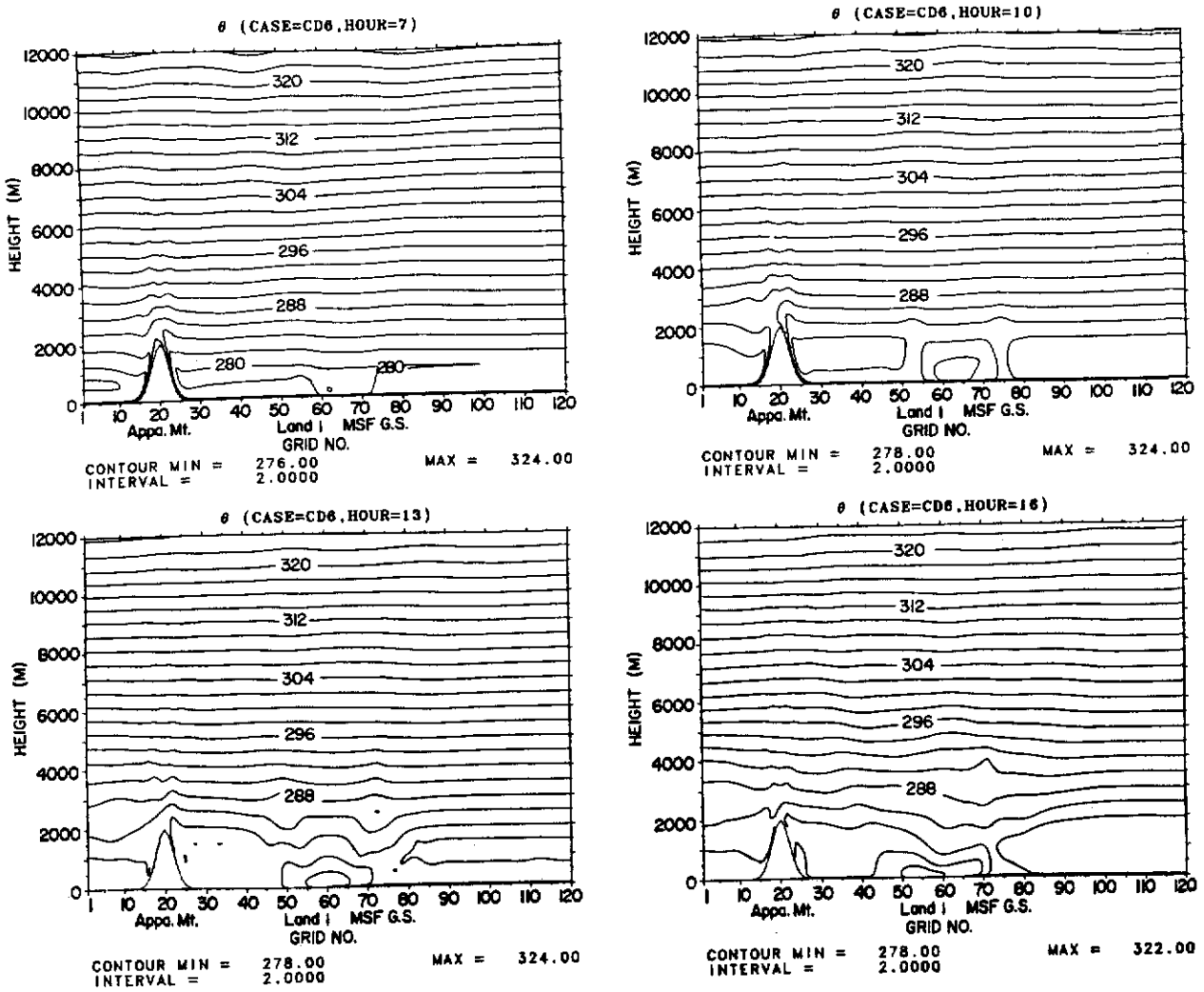

FIG. 3. As in Fig. 2 except for a weak onshore flow for case CD6.

corresponds to the time of maximum ground temperature as will be shown later. This symmetric thermal structure is caused by the nearly equal heating over the coastal plain and the midshelf front region at this time. Surface heat fluxes in these two regions are approximately the same and will be presented in a later section. By 2100 LST, as the nocturnal ground cooling occurs, the circulation over the ocean intensifies and dominates the one near the coastal plain (also see Fig. 15). East of the region of the circulation, the MBL remains neutral. Comparing the results for cases CD1 and CD6, one finds that the different speeds of the ambient flow produce considerably different thermodynamic structures over the entire region. The upstream tilting mountain waves found in CD1 are much weaker in CD6 and the mountain induced circulation is limited to the lowest 3–4 kilometers due to a weaker ambient wind in CD6. By 2100 LST, the maximum mixing height of the MBL to the east of the Gulf Stream is about 2 km. Thus, a ratio of 4 between the two ambient flow speeds for cases CD1 and CD6 does not cause a ratio of 4 in the maximum developed heights of the mixing layer. This ratio is close to one and a half in rough conformity with the ratio of their surface heat fluxes.

For the offshore flow, one would expect the MBL to increase downwind of the baroclinic zone as the flow in this case is across increasing SST contours. Figure 4 shows the potential temperatures for cases CA1 (strong offshore flow) and CA2 (weak offshore flow). The fully developed MBL after 10 hours of integration shifts farther downwind for the stronger offshore flow case as compared to the weaker one. During the period, 1500 LST (model hour 10) to 1800 LST (model hour 13), the circulation front in CA1 as indicated by the fully developed MBL is moving at an average speed of about 30 km h^{-1} ($\sim$8.3 m s^{-1}) in contrast to the very slow movement (near stationary) in CA2. The circu-

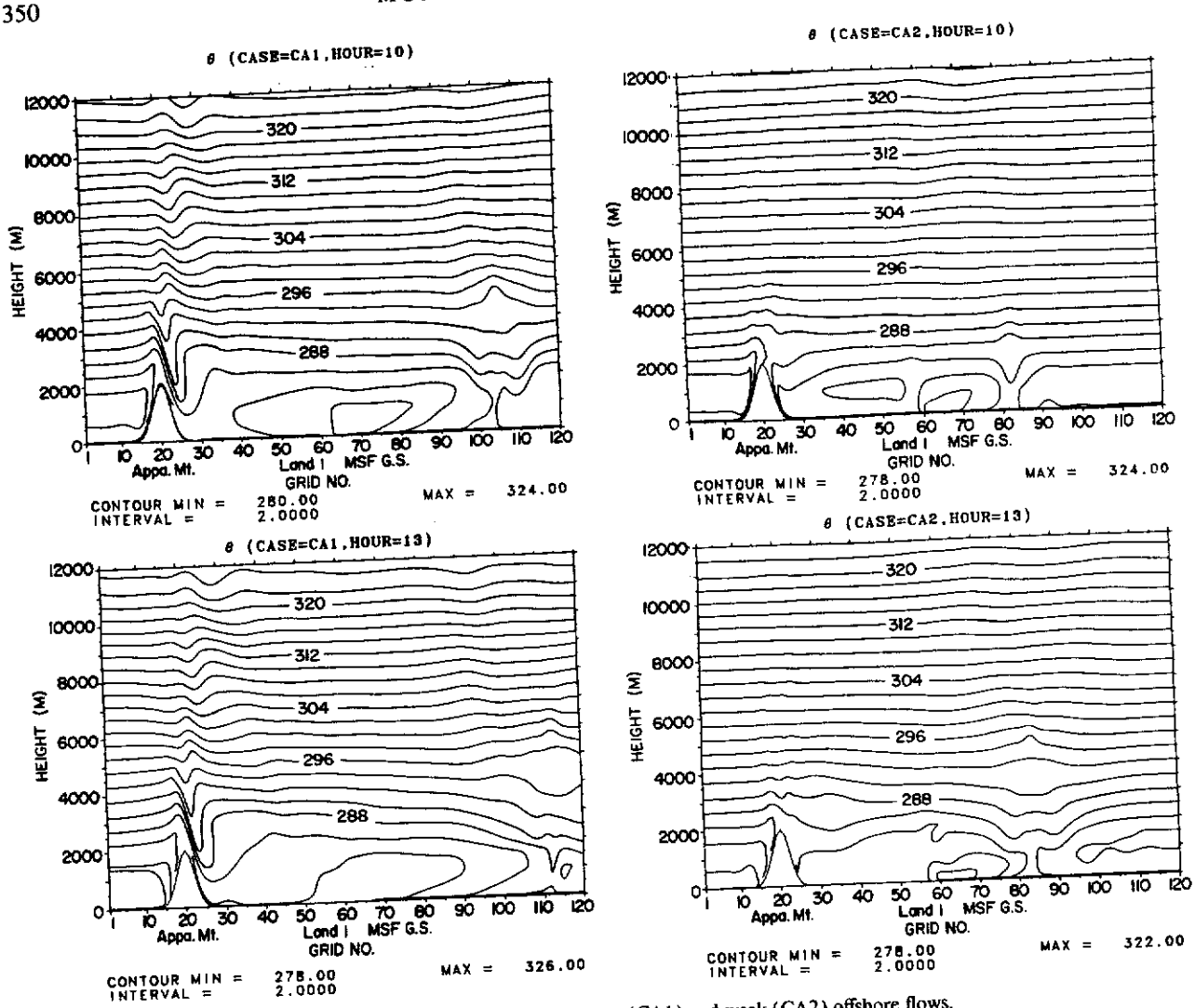

FIG. 4. As in Fig. 2 except for the strong (CA1) and weak (CA2) offshore flows.

lation front moves downstream with a slower speed than the ambient flow, as predicted by Lin and Smith (1986) for a uniform flow over a steady heat source. This is believed to be due to the divergent flow at higher levels in such circulations.

By 2100 LST (model hour 16), the boundary layer over the western side of the mountain has become stable (not shown) but the layer over the eastern side of the mountain remains unstable due to the adiabatic warming of the air as it descends. The PBL structure for the weak offshore flow (CA2) is similar to the weak onshore flow case (CD6); however, the circulation has moved farther offshore to the location of the midshelf front.

Comparing Figs. 2, 3 and 4, one may find that strong ambient flow initiates a deeper MBL and stronger updrafts, while weaker flow produces a somewhat suppressed MBL during the earlier stages of the development of the circulation. Difference in the thermal structure of these MBLs, however, decreases with time as they begin to develop fully in association with the cloud formation. But, the role of the ambient flow direction appears to be more important than its speed in the later stages of the development of the MBL. Stronger ambient flow accelerates the development of the MBL, which in turn results in stronger updrafts reaching to higher levels. This is clearly in contrast to sea breeze circulations in which a strong ambient flow (offshore) suppresses the breeze development. The predicted flow pattern induced by the persistent oceanic baroclinic front, however, is marked by convective instability associated with the cloud development.

It appears that the effects of the large thermal gradients in this study, rarely encountered in sea and land breeze simulations, dominate the MBL. As a result, the fully developed MBL becomes quasi-stationary in the vicinity of the Gulf Stream for the onshore flow but becomes much more transient and moves far

downwind of the Gulf Stream edge for the offshore flow.

In this section, the basic thermodynamic structures for the onshore and offshore flows were presented to lay groundwork for the discussions on other effects in later sections. Before presenting the model results on the wind fields and the mesoscale rainbands, it would be appropriate to discuss the effects of the diurnal ground heating, subgrid cloud heating and atmospheric radiation cooling on the thermal structure. This will help in understanding the sensitivity of the model results to important physical mechanisms.

b. Diurnal variation of the ground temperature

Diurnal variations of the ground temperature obtained using method I [Eq.(19)] at locations A: grid 2, B: grid 20 (mountain top), C: grid 39 (coastal plain), and D: grid 59 (coastal region) for the onshore flow cases CD1 and CD6 are shown in Fig. 5. The ground temperature is a well-defined sine function. Smaller maximum ground temperatures occur with stronger flows. The ground temperatures on the mountain top (B) are smaller for all cases as expected. Larger turbulent transfers in stronger flows obviously help in distributing the net heat to the air and thus reduces the ground temperature. For the weaker onshore flow (case CD6), ground temperatures over the coastal region increase inland, with a maximum difference of approximately 3°C. This is particularly true after continued solar heating and surface layer mixing (1000 LST) and is obviously caused by the mixing of relative cooler air near the coastline with the warmer air over the adjacent land. The ground temperature at the western side of the mountain (A) is greater than that at the eastern side of the mountain (C) after 1000 LST (model hour 5) because of the adiabatic warming. Diurnal variation of the ground temperature for the offshore flow (not shown) is similar to that for the onshore flow.

Although the diurnal heating causes a warming of about 15°C in the ground temperature, the thermodynamic structure of the boundary layer over water is only slightly influenced as shown in Fig. 6 for strong onshore flow cases CD3 and CD4. For CD4 (no diurnal effects), the MBL is almost identical to that in CD1 with diurnal effects computed by the more complicated method II. Case CD3 with diurnal effects computed by the simpler method I shows very similar results (Fig. 2). Removal of the diurnal effects in CD4 has considerably deepened the trough of the mountain waves (Fig. 6), resulting in stronger downslope downdrafts.

c. Radiation and subgrid cloud effects

An understanding of the relative importance of the atmospheric radiation and the subgrid-scale cloud effects would be helpful in determining the degree of physics that a mesoscale model needs. Figure 7 shows the variation of the atmospheric radiation effects

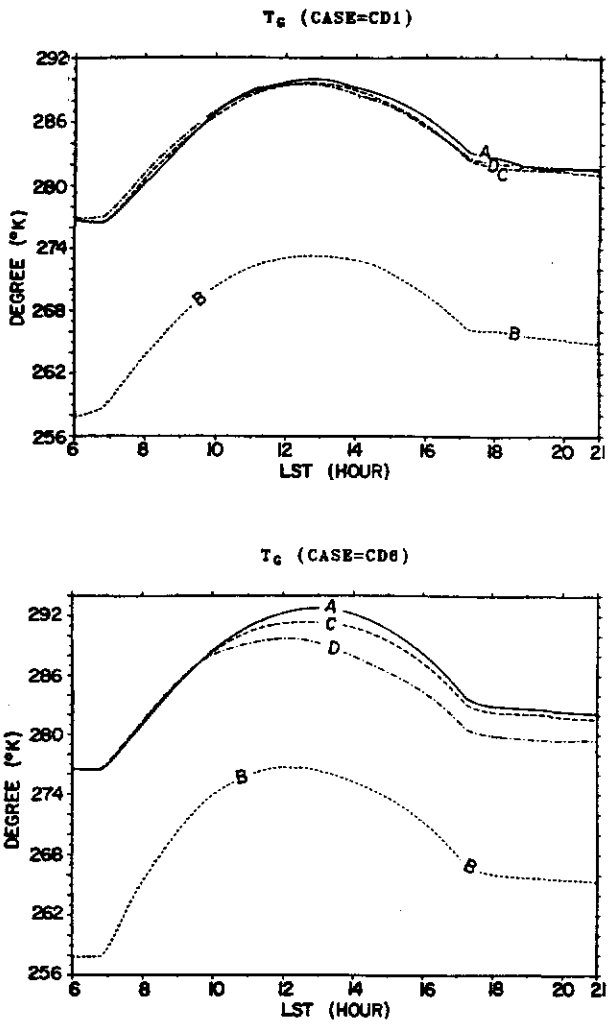

FIG. 5. Variation of the ground temperature with LST at grids 2, 20, 39, and 59, which are indicated by solid line with A, dotted line with B, dashed line with C and dotted–dashed line with D, respectively.

(cooling or heating rate) with LST. The domain maximum atmospheric cooling rate due to longwave radiation over the entire domain is found to be only 1° to 2°C day^{-1}. The domain maximum atmospheric softwave radiation heating is about equal to the cooling by longwave radiation. The domain maximum atmospheric longwave radiation heating rate could reach nearly 3°C day^{-1} (about 0.15°C h^{-1}), but is limited to the surface layer over the Gulf Stream. Thus, there appears to be a net atmospheric longwave radiation heating over the warm ocean. The decreasing magnitude of the longwave heating with time is believed to be caused by the reduction in the air–sea temperature difference as the MBL gets increasingly mixed. From Fig. 5, the atmospheric radiation cooling over land is not able to assist in returning the air temperature to the exact phase of the previous day because of the strong daytime solar ground heating. A sophisticated radiation

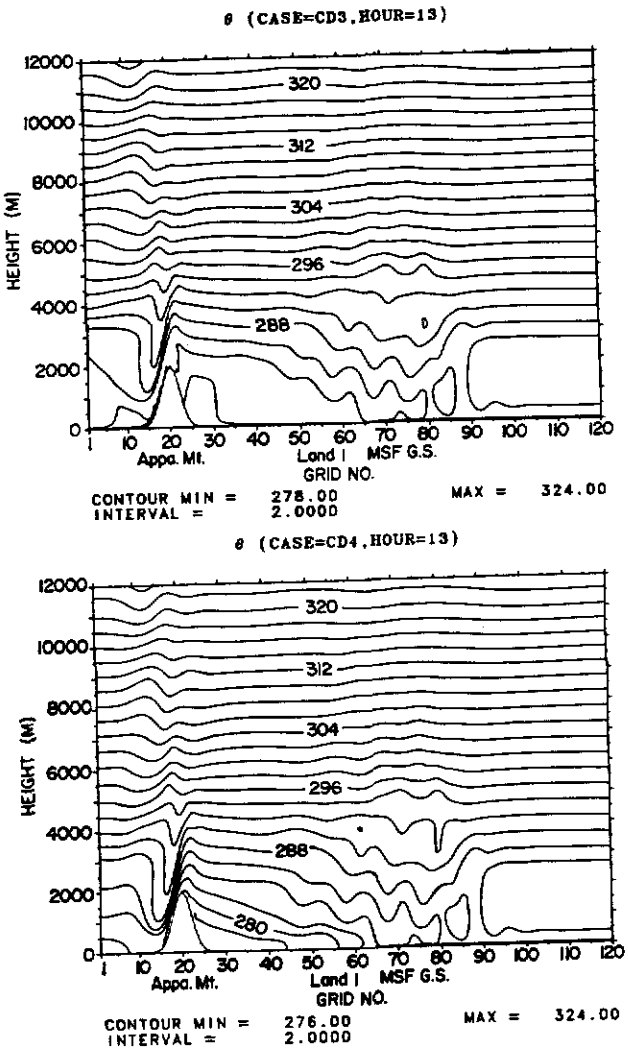

FIG. 6. As in Fig. 2 except for cases CD3 (with method II for diurnal ground heating) and CD4 (without diurnal effects).

scheme that includes the cloud effects may give a longwave cooling rate of the order of 10°C day^{-1} (Pielke 1984). It would be still less than the subgrid cloud heating rate and much less than the surface heating rate by the Gulf Stream as will be discussed in section 4d. Incoming upstream cold air from the lateral inflow boundary could also assist in balancing the increase in energy over the warmer region.

The subgrid cloud heating is much stronger than the radiation effects in each run for cases CD2 and CD7 as can be seen from Fig. 8. The subgrid cloud effects are more pronounced in the oceanic region east of the Gulf Stream front. A region of cloud overshooting to 6–10 km heights and some up to the tropopause is indicated by the negative cloud heating rate. The maximum active cloud height is bounded within the tropopause due to the very dry upper level condition assumed in this study. On the other hand, since the relative humidity of the atmosphere over the ground is set at a constant 80% with respect to the ground temperature, subgrid clouds do not develop over land except over the region affected by the local breeze (case CD7). Constant relative humidity assumed for the ground limits the application of this model to some particular atmospheric conditions such as the flow over the moist land surface. Comparing the results of 1800 LST (model hour 13) with those at 2100 LST (model hour 16), the far upwind region becomes more favorable for the occurrence of the subgrid clouds due to the increase in convective instability in a fully developed MBL. The warm SST and the upward moisture transport over the ocean are thus very important for the cloud formation and growth. In Fig. 8, the subgrid cloud heating rate has a maximum magnitude of about 24°C day^{-1}, at a height of about 6 km for case CD2 with the stronger onshore flow. For the weaker onshore flow (case CD7), the subgrid clouds reach about the same height but the heating rate is lessened by about a factor of two. Both cases indicate that the active core of the subgrid clouds is approximately stationary with a cloud free region between the two major cloud groups. We will show in section 4e that the cloud free region is a downdraft region.

The strong subgrid cloud heating, however, does not seem to cause a significant change in the MBL thermodynamic structure. This is illustrated by comparing case CD2 in Fig. 9 to CD1 without subgrid cloud effects (Fig. 2). It is apparent that the lower part of the MBL remains almost the same except over the western edge of the Gulf Stream. Here the potential temperature field from the upper part of the MBL to the middle troposphere is slightly modified by the subgrid cloud

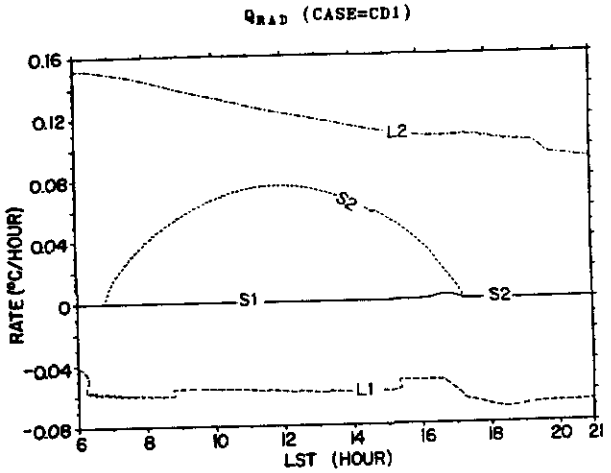

FIG. 7. Temporal variations of the domain maximum and minimum radiation heating rates with LST for the strong onshore flow (case CD1). Solid line (S1), minimum shortwave radiation heating; dotted line (S2), maximum shortwave radiation heating; dashed line (L1), minimum longwave radiation heating; dotted–dashed line (L2), maximum longwave radiation heating.

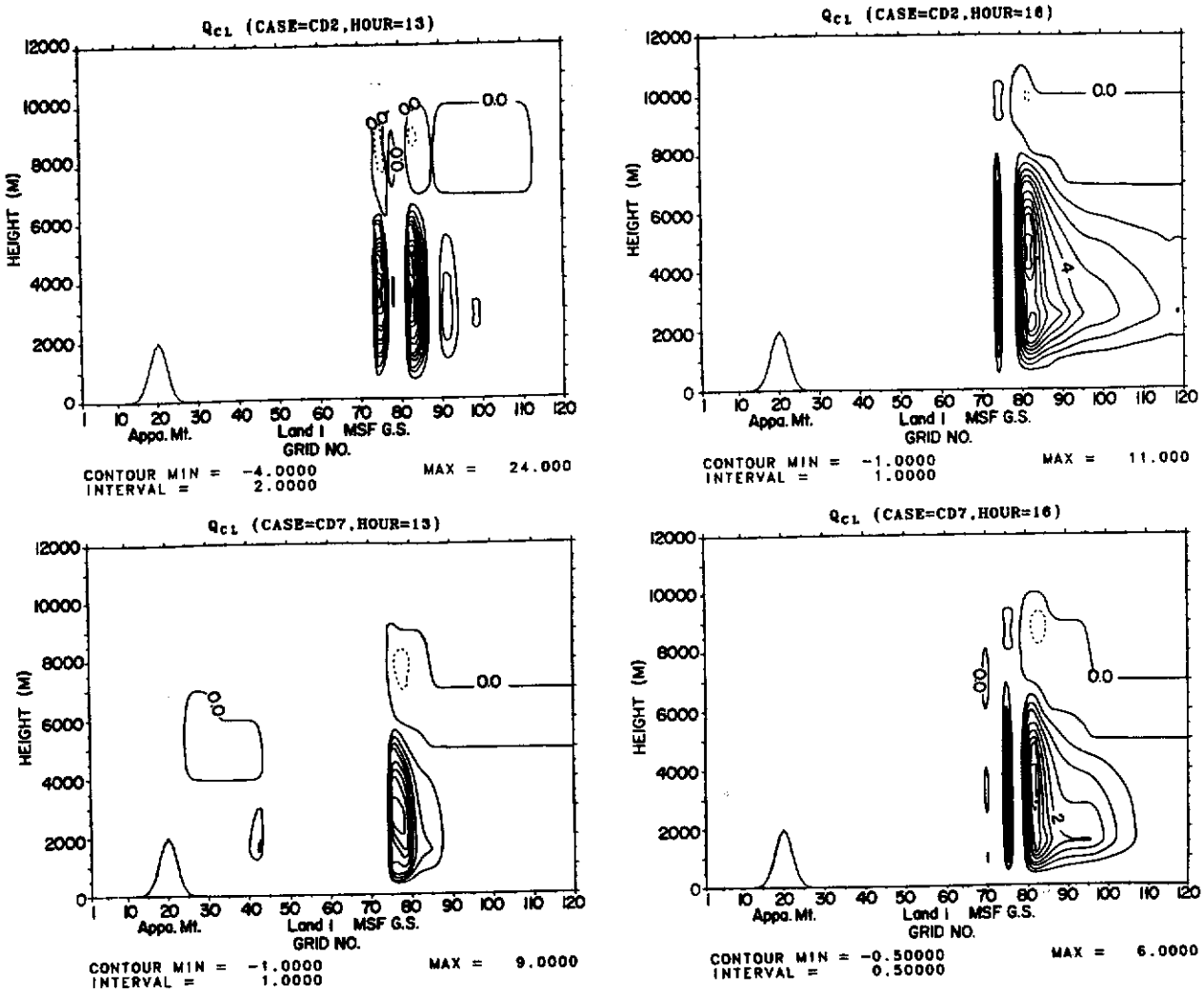

FIG. 8. Subgrid cloud heating for the onshore flow for cases CD2 (strong) and CD7 (weak). Unit of contours in each panel is °C day^{-1}.

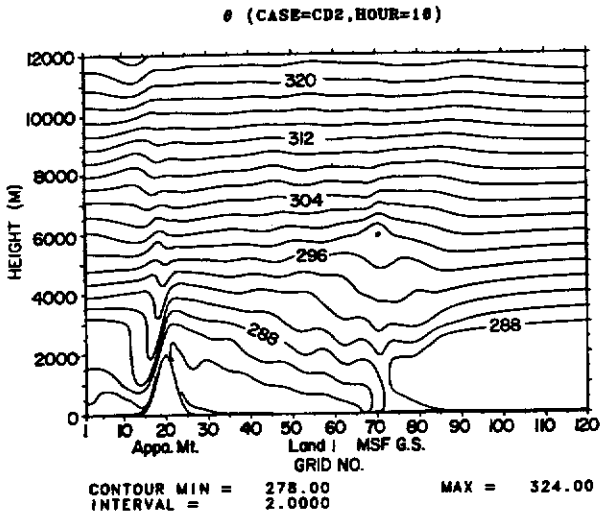

FIG. 9. As in Fig. 2 except for case CD2 (with subgrid cloud effects).

effects. Heating rates of the lower levels in the MBL over the region of the Gulf Stream are so strong due to the high surface turbulent transfer that other effects such as the strong subgrid cloud heating and the atmospheric radiation become relatively less important. Characteristics of the vertical turbulent transport in the surface layer are discussed in section 4d.

d. Turbulent exchange in the surface layer

The vertical turbulent transport under different stability conditions can be characterized by the amount of turbulent exchange and transfer within the surface layer. The spatial variations of the surface friction velocity u_* at different times for cases CD1, CD6, CA1 and CA2 are shown in Fig. 10 for the onshore and offshore flows. In the figure, numbers indicate LST. In general, the friction velocity is larger (by a factor of up to four) for the cases with the stronger flows as one

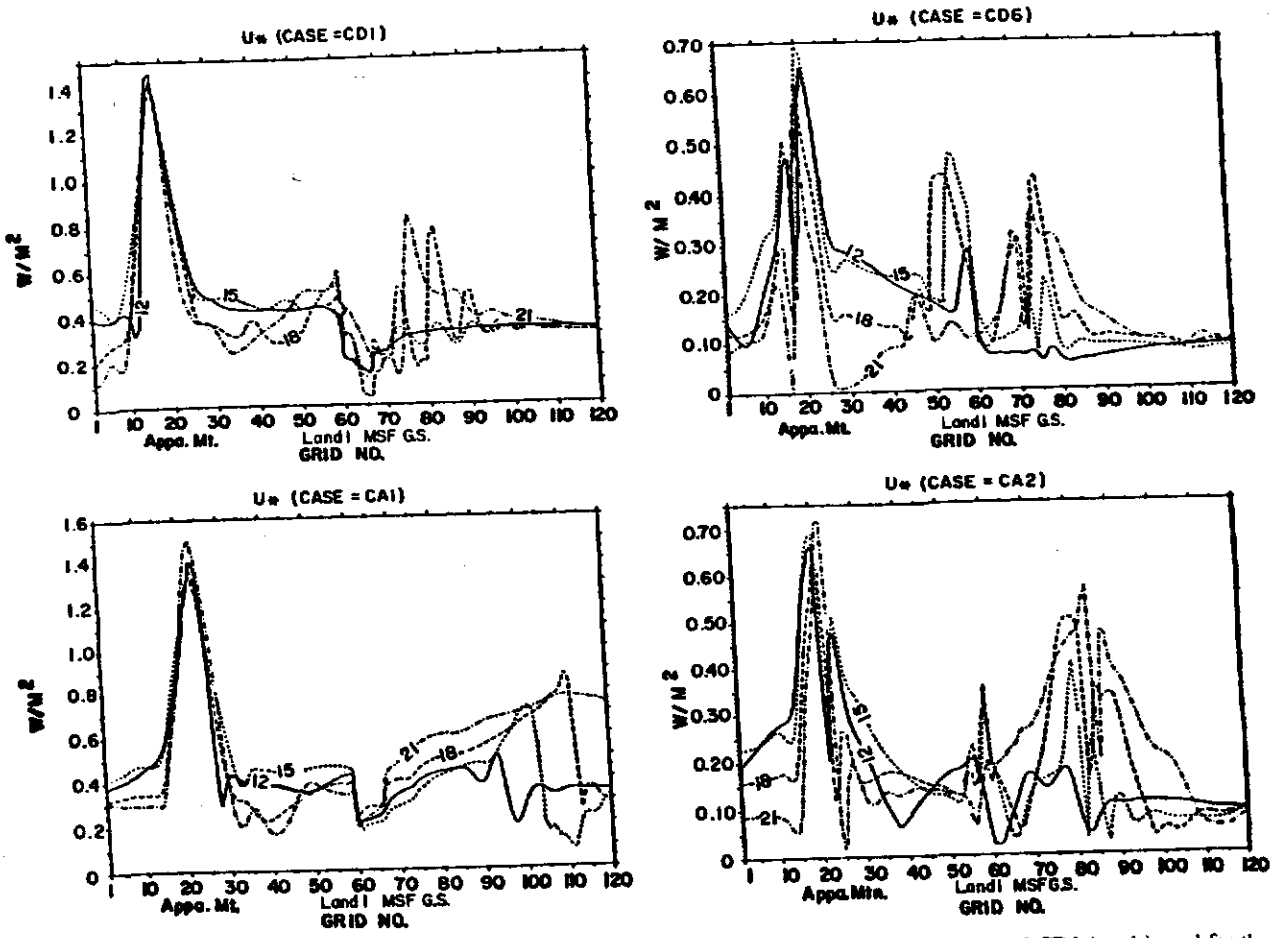

FIG. 10. Spatial variation of surface friction velocity (u_*) for the onshore flow for cases CD1 (strong) and CD6 (weak), and for the offshore flow for cases CA1 (strong) and CA2 (weak). Solid line (12), 1200 LST (model hour 7); dotted line (15), 1500 LST (model hour 10); dashed line (18), 1800 LST (model hour 13) and dotted–dashed line (21), 2100 LST (model hour 16). Symbols in the bottom of each panel represent locations as in Fig. 2.

would expect, irrespective of the ambient wind direction. At the downwind side of the mountain, the katabatic flow produces higher momentum; hence high u_* occurs for both CD1 and CA1 for the stronger ambient flows. In both CD6 and CA2, with the weaker flows, the maximum u_* is found at the upwind side of the mountain during the daytime. This maximum turbulent momentum transport is consistent with the relatively stronger mixing during the day. In general, the maximum u_* over the ocean is associated with the MBL development, but over land it mainly depends on the degree of diurnal ground heating. The surface layer momentum exchange over the ocean in each case is not significantly high compared to that over the land regions, except for the large values over the regions of low level convergence.

In case CD6 with weaker onshore flow, two major peaks of u_* are associated with the two sea breeze types of circulation discussed before (Fig. 3). One of these occurs over the ocean due to strong SST gradients and the other over land due to the solar heating. For the cases with offshore flow, the shifting of u_* maxima primarily follows the movement of the circulation front (see Fig. 4). Despite the very warm SST over the Gulf Stream, the maximum u_* for offshore flows does not appear near the western edge of the Gulf Stream but occurs farther downstream after the MBL has fully developed. A comparison of the values of u_* for the onshore and offshore flows indicates that the momentum exchange is direction-dependent through the SST variation and inherent baroclinicity. This exchange in turn produces differing thermodynamic structures (see Figs. 2, 3, and 4).

Variations of the sensible and latent heat fluxes for cases CD1 and CD6 for onshore flow are shown in Fig. 11. One common feature is that the surface latent heat flux over the ocean is two to three times the surface sensible heat flux, in agreement with the observations during the GALE IOP 2 (Akkarapuram and Raman 1988). Over the ocean, variations in the surface tur-

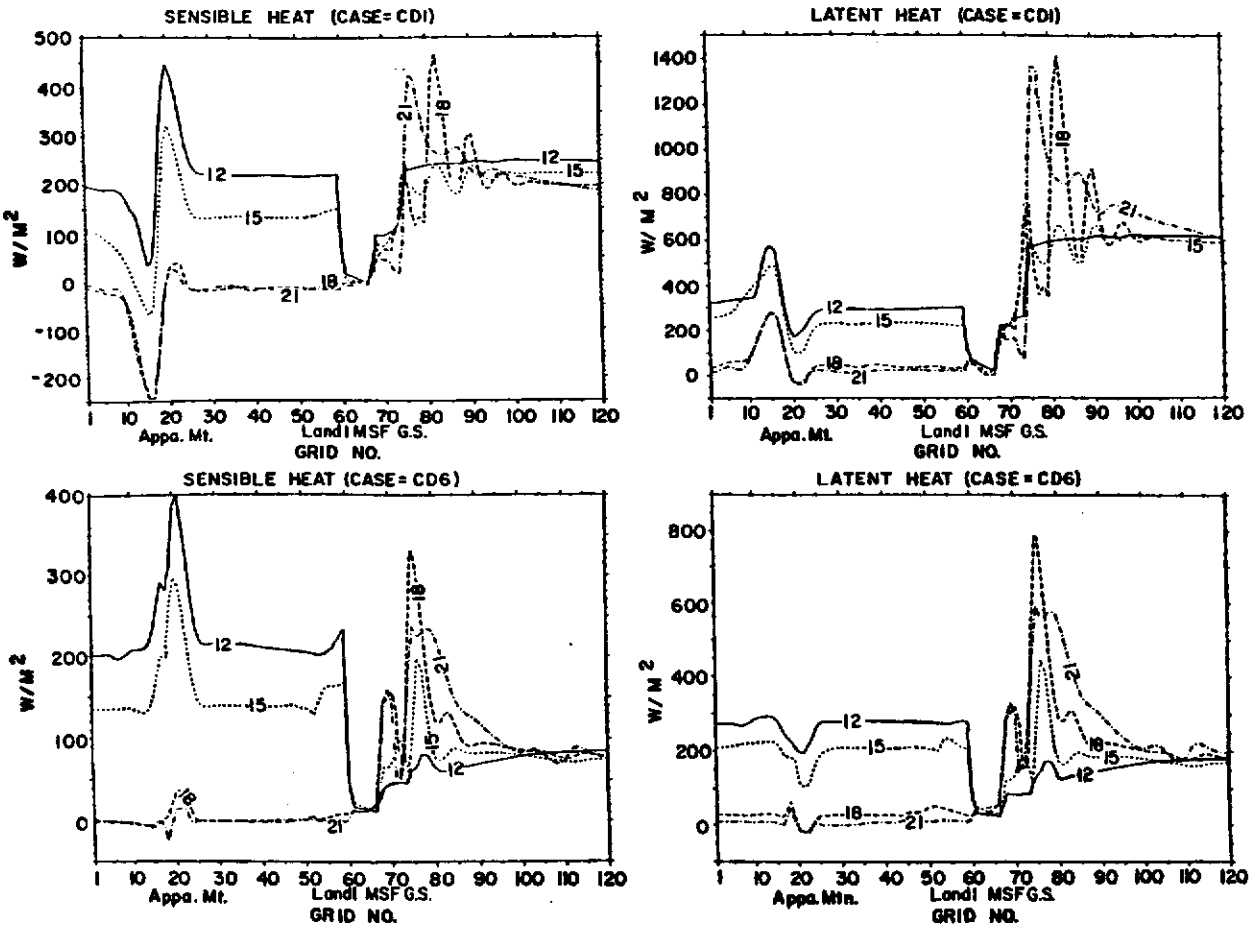

FIG. 11. As in Fig. 10 except for the variation of the surface turbulent sensible and latent heat fluxes for the onshore flow cases CD1 (strong) and CD6 (weak).

bulent heat flux are similar to the variations of the turbulent momentum exchange since the surface layer is homogeneous and highly convective. Also, over the oceanic region the convective velocity (w_*) is quite high with a maximum value of about 4 m s^{-1} (not shown).

Heat flux over land for the onshore flow cases reaches a maximum near 1200 LST (model hour 7), indicating the importance of the diurnal heating in determining the total amount of surface heat flux; however, this is not the case for u_*. For example, the maximum u_* at 1800 LST (model hour 13) near the coastline for case CD6 (with the weaker onshore flow) does not correspond to a maximum surface heat flux but to a value close to zero. This is due to near neutral condition of the surface layer at 1800 LST (model hour 13) near the coastline.

The wind over the western side of the mountain in case CD1 (with the stronger onshore flow) exhibits a minimum (and sometimes even downward) sensible heat flux, although the associated u_* is maximum. The small downward moisture flux appearing over this region during the night (1800–2100 LST) is due to the assumption that the relative humidity over the cooled ground is constant. This results in a smaller surface moisture than the modified upper level moisture. On the other hand, the larger latent heat flux on the eastern side of the mountain is due to the cooling of the ascending flow. Both surface sensible and latent heat fluxes over the ground have maximum values near noon (1200 LST), while the maximum values over the ocean appear around 2100 LST (model hour 16). For the offshore flows the spatial distributions of fluxes of latent and sensible heat over the ocean are similar to their u_* distribution.

Fluxes of latent and sensible heat over the regions of the Gulf Stream and the midshelf front were found to be at least 500 W m^{-2}. The maximum value of the total heat fluxes for the cases with the stronger flow (both onshore and offshore) reaches a value of about 1800 W m^{-2} near the western edge of the Gulf Stream. Even for the cases with the weaker flow, the maximum

value of the total heat flux still exceeds 1200 W m^{-2} for the offshore flow and 1100 W m^{-2} for the onshore flow. Thus, the total heat flux over the Gulf Stream does not seem to depend on the direction of ambient flow but on the flow speed. Our modeling results for the total heat fluxes are in agreement with the observations during GALE (Raman and Riordan 1988; Akkarapuram and Raman 1988; Wayland and Raman 1989) and other experiments (Chou and Atlas 1982).

e. *The Gulf Stream rain bands and convergence zones*

A major objective of this study is to investigate the geometry of the Gulf Stream-induced convergence zones and the accompanying rainbands and/or cloud bands. Figure 12 shows the computed liquid water contents for cases CD1 and CD6 for stronger and weaker onshore flows respectively at 1800 LST (hour 13) and 2100 LST (hour 16). Liquid water is found to appear predominantly over the oceanic region for case CD1. The liquid water occurring over the upwind slope of the Appalachian Mountains is associated with orographic rain (Smith 1979). Major oceanic rainbands occur at 1800 LST for case CD1. In this study, precipitation is assumed to occur when liquid water exceeds 1 g kg^{-1}. In case CD1 (Fig. 12), rainbands are found to correspond to the three SST jumps shown in Fig. 1. At 2100 LST, the coastal cloud band disappears due to the ground cooling as the PBL becomes stable at the coastal region. Also, the two rainbands near the midshelf front merge and become quasi-steady close to the western edge of the Gulf Stream.

It is interesting to note that for case CD6 (weaker onshore flow) the mesoscale structure of the cloud bands (the liquid water loading not greater than 1 g kg^{-1}) is quite different at 1800 LST from the stronger onshore flow case (CD1). A cloud band that occurs inland at 1800 LST due to ground warming disappears

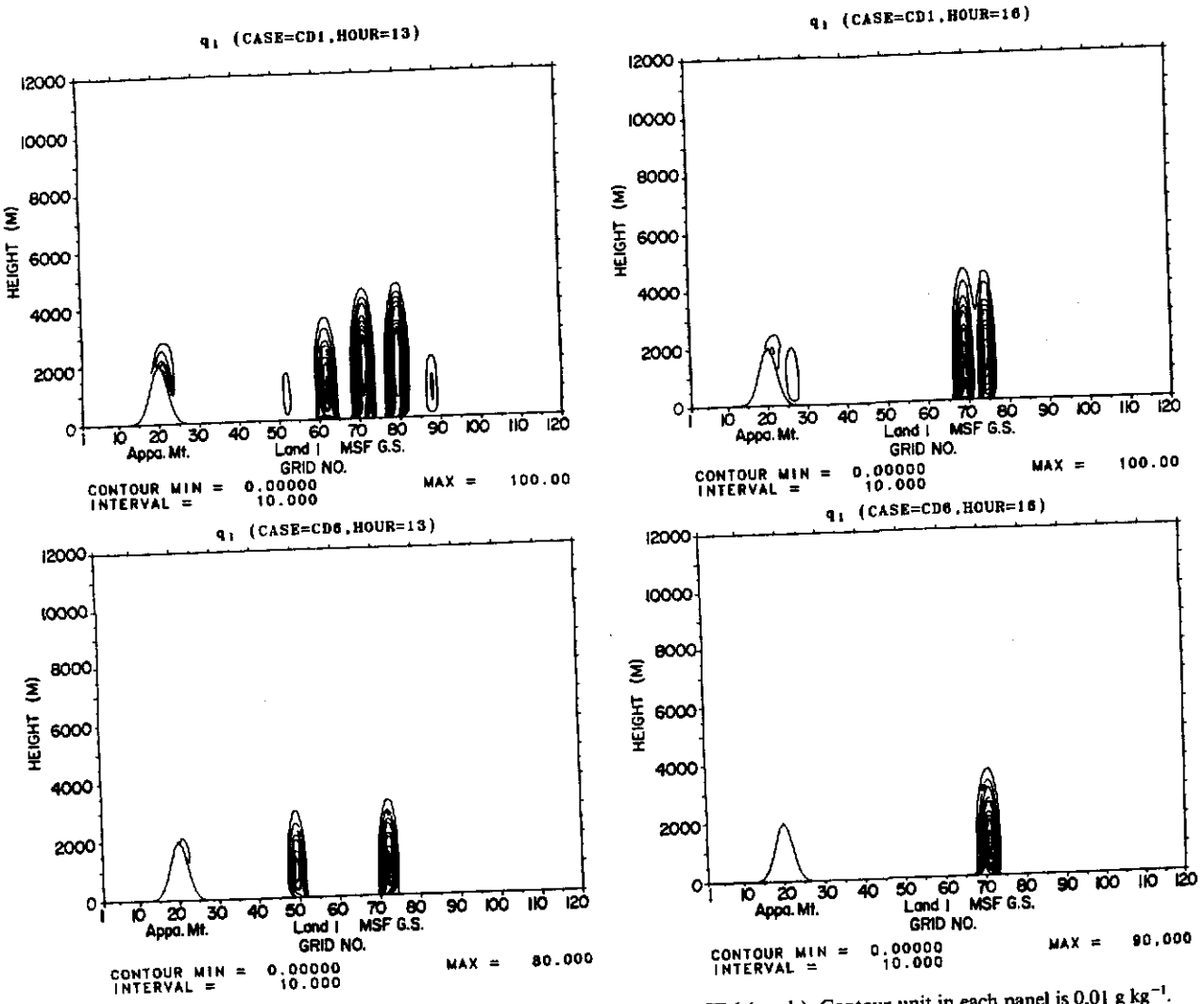

FIG. 12. Liquid water content for the onshore flow cases CD1 (strong) and CD6 (weak). Contour unit in each panel is 0.01 g kg^{-1}.

at 2100 LST. Only one major cloud band is observed over the midshelf front downwind of the western edge of the Gulf Stream.

For the offshore flow, the major cloud band, however, occurs downwind of the Gulf Stream (Fig. 13), consistent with the thermodynamic structure (Fig. 2). With the stronger offshore flow (case CA1), the rainband forms further downwind. At 2100 LST, the rainband pushed by the strong offshore flow moves out of the model domain, while the one in CA2 (with the weaker onshore flow) remains in the same region. The movement of the circulation front can be retarded or completely eliminated by the offshore flow produced by the SST gradients. Thus, the oceanic cloud bands appear downwind of the Gulf Stream for the onshore flow. For offshore flows, however, the situation is reverse with the ambient flow in the direction of the baroclinicity, resulting in the geometry of a single rainband. Comparing the vertical cross sections of the clouds for each case, we find that the stronger flow produces taller clouds (~5 km height) despite the flow direction. The taller clouds are caused by the more intense updrafts induced by the stronger surface turbulent heat fluxes (see Figs. 14 and 15). The heights of rainbands for the onshore flows are slightly less than that for the offshore flows. This could be due to the advection of relatively colder air over a limited oceanic fetch thus maintaining a larger air–sea temperature difference. For CA1 with the stronger offshore flow, the modeled rainband of about 5–6 km height is consistent with those presented by Sienkiewicz et al. (1989) for a large scale cyclone moving offshore.

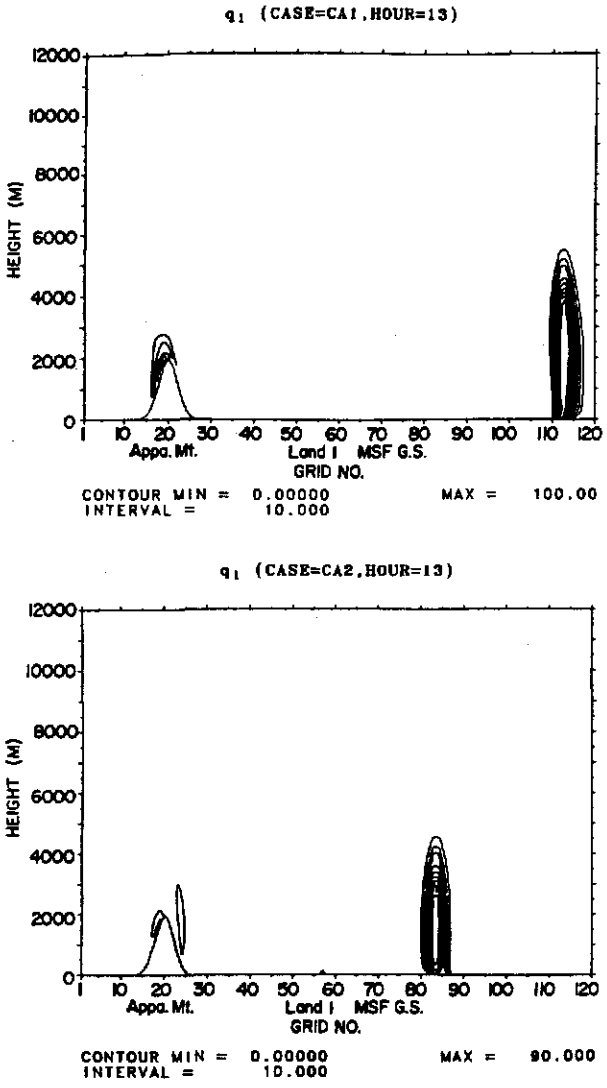

FIG. 13. As in Fig. 1 but for the offshore flow cases CA1 (strong) and CA2 (weak).

The distributions of grid and subgrid precipitation were also investigated. As mentioned before, the precipitation in the model can occur only when the liquid water exceeds 1 g kg^{-1}. Thus, precipitation appears only after the clouds have formed. The maximum subgrid precipitation (~3.7 mm) for case CD2 and (~2.4 mm) for case CD7 are not negligible compared to the maximum total grid precipitation (~7 mm). Peaks of the subgrid precipitation are in correlation with those of the grid precipitation but lag the grid clouds to the east and are also much wider. This result agrees with the distribution of the subgrid clouds. Also, the grid scale precipitation in both cases increases when the subgrid clouds are taken into account. This is caused by the stronger updrafts that develop in response to the release of additional subgrid latent heat.

The simulated rainbands with a typical width of 70 km (for both onshore and offshore flows) are located about 70 km apart (for onshore flow) and are related to the convergence zones near SST discontinuities. The diverse geometries of the rainbands for the onshore flow cases can be better understood by an inspection of the wind fields. Figure 14 shows the wind fields for case CD1 (stronger onshore flow) at 1800 LST (hour 13) and 2100 LST (hour 16). In order to have a better resolution, wind vectors over land and ocean are presented separately since the downslope wind usually has a much larger vertical motion than that in the circulations over the ocean. The ground heating causes an increase in the Froude number and enables slightly more flow over the mountain at 1800 LST and 2100 LST. No intense flow convergence occurs over the coastal plain during the night.

As expected, comparing the results shown in Figs. 12 and 13, one can find that the geometry of the rainbands is essentially determined by the low-level flow convergence. For example, one of the three low level convergences adjacent to the coastline disappears at 2100 LST, in correspondence with the disappearance of the coastal rainband. The onshore movement of the most upwind rainband in Fig. 12 is also closely related to the inland penetration of the associated updraft. For

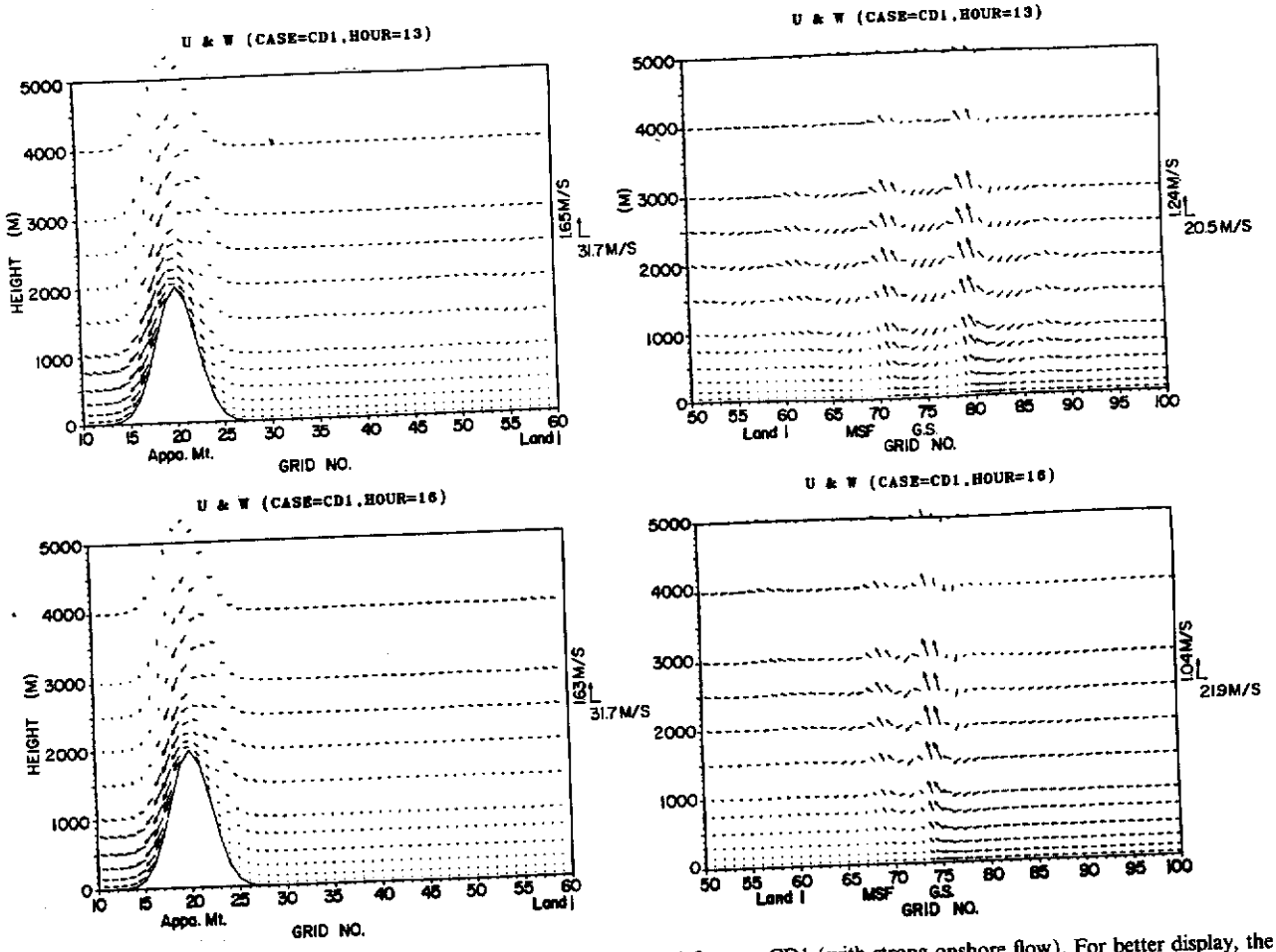

FIG. 14. East–west wind component (u) and vertical component (w) for case CD1 (with strong onshore flow). For better display, the wind fields over land and sea are plotted separately. The wind vector is stretched by a ratio of 2 in scaling maximum w with respect to maximum u. Maximum u and w are plotted right of each panel.

case CD6 (weaker onshore flow), there are two major convergence zones at 1800 LST, one over the coastal area and the other near the Gulf Stream, as shown in Fig. 15. At 2100 LST, the inland one disappears, while the other persists. The wind over the eastern side of the mountain gets stronger at 1800 LST for case CD6 due to the ground heating. The flow becomes weaker at 2100 LST. General features of the wind fields are consistent with the symmetric structure of the circulations and the cloud bands (Fig. 15). The maximum wind speed regions caused by the flow convergence ahead of the circulation front is also associated with the regions of the maximum friction velocity u_* (Fig. 10).

f. Influence of the Appalachian Mountains

In order to better understand the role of the Appalachian Mountains in the entire flow regime, simulation of case CD5 without the mountain was performed. Figure 16 shows the across-mountain wind component u, vertical velocity w and potential temperature θ at 1800 LST (model hour 13) for case CD5. In this case, the updrafts have shifted onshore by about 20 km more than for other strong onshore cases CD1 (Fig. 14), CD3 and CD4 (results for the latter two cases are not shown). Also, all major updrafts are somewhat weaker compared to the cases in which the Appalachians were included. Propagation of the upstream influence of the mountain moves the oceanic rainbands further offshore and leads to stronger updrafts which in turn lead to changes in the upper level structure of the MBL.

Comparing Figs. 2 and 16, one can conclude that the low levels of the MBL in the vicinity of the Gulf Stream and the mixed layer upwind of the Gulf Stream, however, are not significantly affected by the upstream influence of the mountain. But, the fully developed MBL height is suppressed by about 1 km for the case without the mountain. The upstream influence of the mountain over the coastal ocean appears to be offset by the presence of the mesoscale circulation in the vicinity of the Gulf Stream. The upstream effect of the

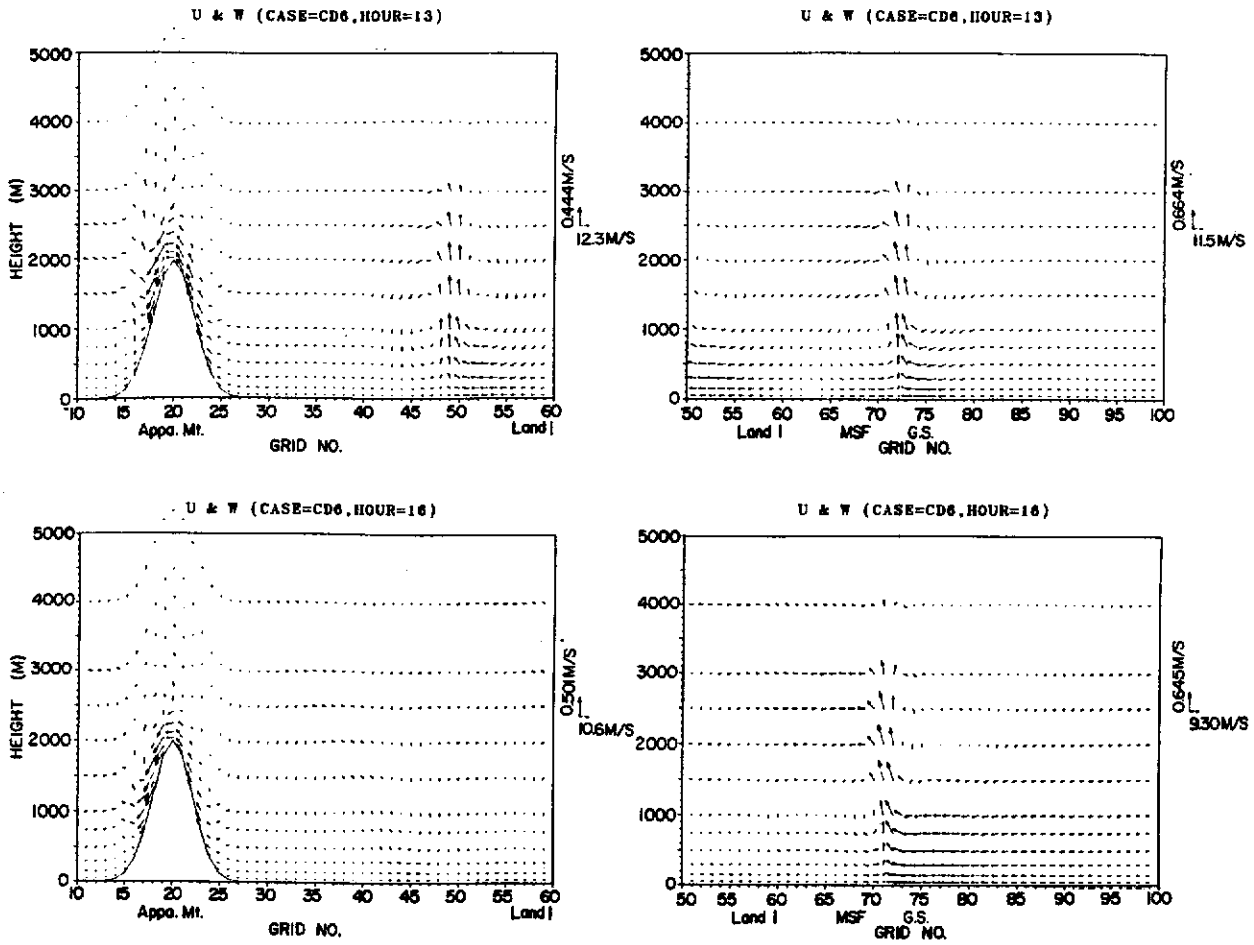

FIG. 15. As in Fig. 14 except for case CD6 (with the weak onshore flow).

Appalachian Mountains thus does not change the general structure of the MBL and the rainband pattern, although it has some influence on individual major updrafts. This is partly because the Appalachian Mountains are far (400 km) from the oceanic region, and partly because the surface heating dominates the thermodynamic structure of the MBL as compared to the dynamical forcing by the mountain.

Cold air damming, another effect of the mountain, is associated with an increased southward wind component (Richwein 1980). The along-mountain component, v for cases CD3 (with diurnal effects), CD4 (without diurnal effects) and CD5 (without the mountain) at 1800 LST (model hour 13) are compared in Fig. 17. Initially, the v component is set to be 0.1 m s^{-1}. It appears that the effects of the Appalachian Mountains are to entrench the flow and to divert it more southward as in the dynamics of a barrier wind (Smith 1979; Pierrehumbert 1984; Pierrehumbert and Wyman 1985). The results are only slightly different when the effects of diurnal ground heating are included.

The flow regime has similar flow dynamics as in a shallow stationary front over the oceanic midshelf front (near the western edge of the Gulf Stream) with apparent southwestward along-front wind west of the front and northeastward along-front wind east of the front. Strong ageostrophic wind is produced in the vicinity of the oceanic baroclinic zone as indicated in Figs. 14 and 17. The structure is somewhat symmetric around the leading edge of the front near the region of the midshelf oceanic front at 2100 LST. The upper part of this frontal structure inland is greatly modified by the mountain as compared to that in case CD5 without the mountain. Comparing the results with and without the mountain effects (cases CD3 and CD5, respectively), the southwestward wind in the frontal zone in CD5 without the mountain still has a value of about 12 m s^{-1} as compared to 17 m s^{-1} for CD3 with the mountain. This implies that the effects of just the oceanic baroclinic zone with the diurnal change can result in a strong "cold air damming" type of phenomenon.

The upstream influence of a Gaussian mountain should have a typical length scale of the radius of de-

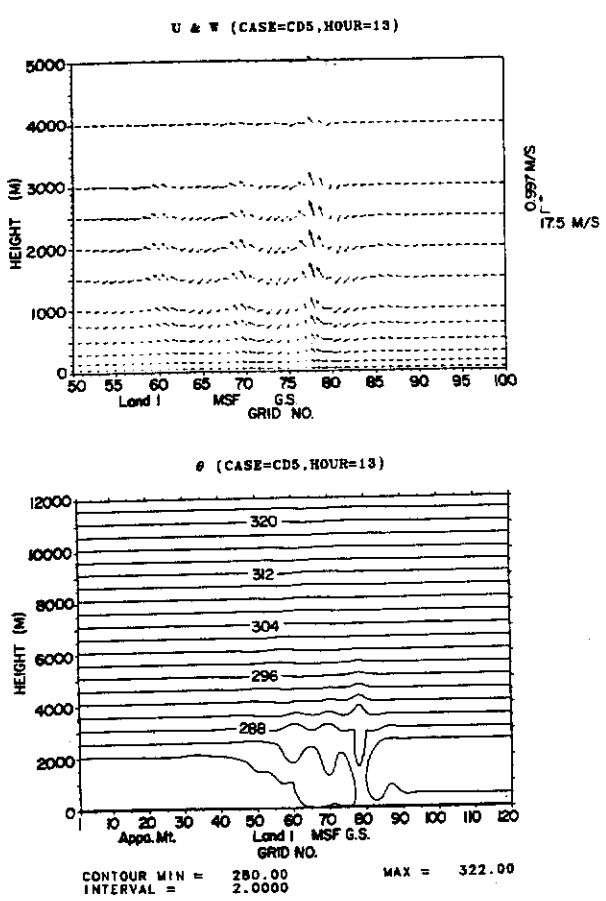

FIG. 16. Wind components (u and w) and potential temperature (θ) at 1800 LST (model hour 13) for the strong onshore flow (case CD5) with the removal of the Appalachian Mountains.

formation Nh/f where h is the mountain height (Pierrehumbert and Wyman 1985). This length scale is about 250 km for the cases with onshore flow in this study (as compared to a distance of 400 km between the Appalachian Mountains and the coastline); hence the mountains should have some influence on the flow over the coastal plain. As shown in the results of cases CD3, CD4 and CD5, the upstream influence of the mountain extends to the oceanic region and causes some modification of the upper levels of the MBL, though the associated mechanism is not clear. The lower part of the MBL, however, appears insensitive to the mountain influence, implying that the effects of the ocean warming controls the dynamics of the MBL.

For the offshore flow, the thermal forcing caused by the oceanic baroclinicity downstream is dominant over the dynamic forcing of the far upwind mountain. Even for a nonlinear hydrostatic flow free of the boundary layer mixing, the mountain influence length scale may not be limited with increasing time (Pierrehumbert and Wyman 1985). In this study, the Appalachians are 400 km away from the coastline, which is about 20 times the mountain half-width, and the distance is much more to the location of the offshore rainband.

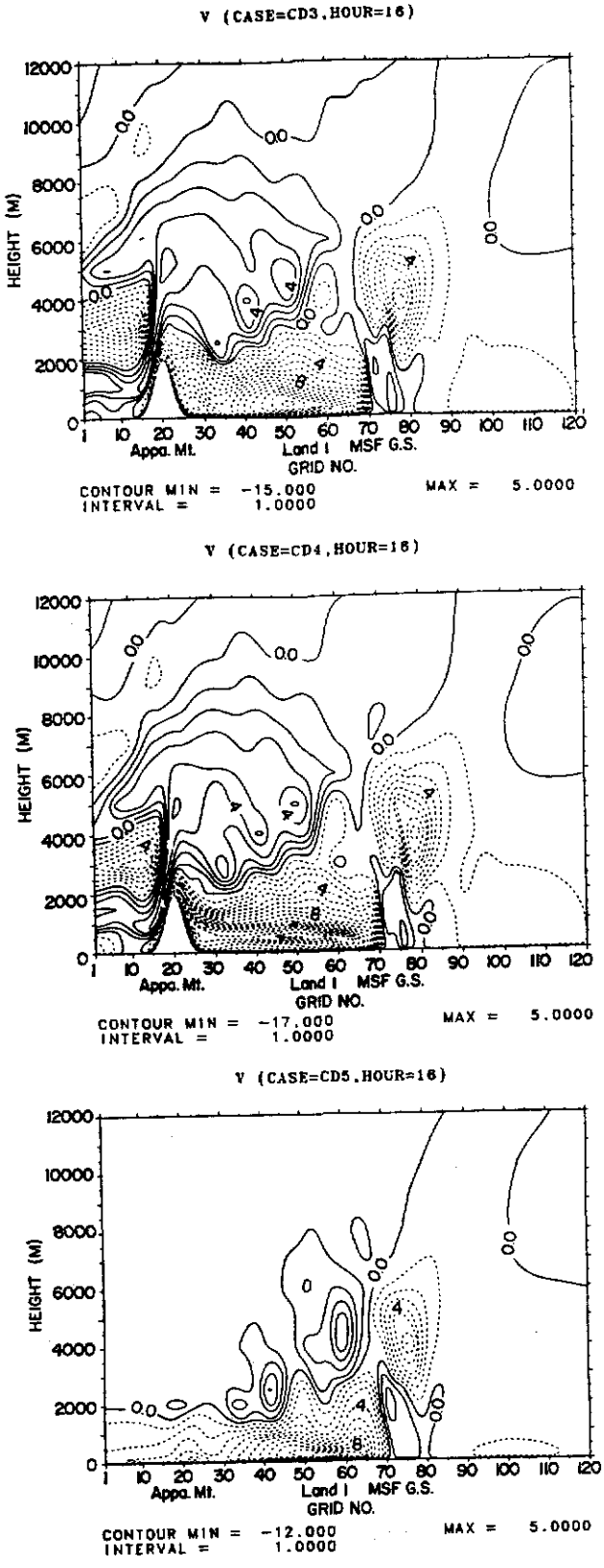

FIG. 17. Wind component (v) along the mountain ridge for the strong onshore flow cases CD3, CD4 and CD5 (see Table 1 for their description). Contour unit is m s^{-1}. The dashed contour lines indicate negative values and the solid contours positive values.

5. Concluding remarks

Several process-oriented numerical experiments were conducted to study the cold air flow modified by mesoscale topography, in particular, the Appalachian Mountains and the oceanic frontal zones off the Carolinas, using a two-dimensional (2-D) mesoscale planetary boundary layer (PBL) model. This model includes diurnal effects, atmospheric longwave and shortwave radiation and subgrid cloud effects. PBL turbulent transfer is modeled by the turbulent kinetic energy (TKE) closure. The simulation time of the cases is chosen from 0500 to 2100 LST for approximate meteorological conditions of IOP-2 of the GALE. Important results obtained in these simulations are:

(i) Effects of strong sea surface heating (for example, up to 50°C day^{-1} warming rate by the sensible heat) are far more important than the subgrid cloud effects with a typical heating rate of about 20°C day^{-1} for the MBL development over the region of the Gulf Stream. The effects of atmospheric radiation are even less with the associated heating or cooling rate of about 2°–3°C day^{-1}.

(ii) The MBL over the Gulf Stream is not sensitive to diurnal heating over land at least during the winter months considered (with a 15°C warming of the ground temperature). Diurnal effects, however, can change the inland flow regime considerably, resulting in a local circulation and the generation of a cloud band.

(iii) The direction of ambient flow is a dominant factor in determining the locations of the most intense updrafts in the MBL. For onshore flow, these updrafts are nearly stationary in the vicinity of the Gulf Stream but move with the mean wind for the offshore flow. With the stronger offshore flow, the MBL becomes deeper and moves farther offshore.

(iv) Over the region of the fully developed MBL, surface turbulent latent heat flux is found to be larger than the sensible heat flux by a factor of about two to three and the combined fluxes are more than 500 W m^{-2} on the average with a maximum value of about 1800 W m^{-2} over the Gulf Stream. The total heat flux over this region depends primarily on the speed of the ambient flow rather than its direction. The maximum momentum flux at the surface layer is associated with the maximum wind ahead of the low level convergence zone.

(v) The formation of the Gulf Stream cloud (rain) bands is in response to the low level flow convergence near the western edge of the Gulf Stream for onshore flow; for offshore flow, the occurrence of a single major cloud (rain) band is in conjunction with the circulation front downwind of the western edge of the Gulf Stream.

(vi) There is some upstream influence of the Appalachian Mountains on the intensity of the updrafts and the MBL structure near the Gulf Stream. This moves the oceanic rainbands further offshore. Downstream influence of the mountain has no significant effect on the MBL because of the large distance that separates them.

(vii) Cold air damming over land can produce a southwestward component up to 17 m s^{-1} for an ambient wind of 10 m s^{-1} for the case with the Appalachian Mountains indicating the entrenchment of the onshore flow. When the mountain is removed in the model, a southwestard wind of 12 m s^{-1} is still present. This is believed to be caused by a shallow front over the oceanic baroclinic zone.

Our 2-D modeled MBL structure for idealized conditions, but over realistic topography, is in qualitative agreement with the observations (Raman and Riordan 1988; Wayland and Raman 1989; Holt and Raman 1990). Direct comparisons between the model results and the observations are not made since all the case simulations are idealized to understand the basic processes. The model simulates tall and narrow rainbands for the offshore flow cases (about 5–6 km in height and 70 km in width) as reported by Sienkiewicz et al. (1989).

Diurnal effects over complex terrain are more difficult to simulate because of the requirements of consistent model initialization using representative sounding data and realistic inflow boundary conditions (e.g., Smolarkiewicz et al. 1988). The results obtained in this study provide a dynamical understanding of the mesoscale features caused by the cold air advection over the GALE region and gives an insight into the associated physical mechanisms of the MBL over the Gulf Stream.

Acknowledgments. The authors would like to thank P. LeMone for very helpful suggestions in improving the manuscript. This work was supported by the Division of Atmospheric Sciences, National Science Foundation under Grants ATM-83-11812 and ATM-88-01650.

REFERENCES

Akkarapuram, A. F., and S. Raman, 1988: A comparison of surface friction velocities estimated by dissipation and iterative bulk aerodynamic methods during GALE. *Geophys. Res. Lett.*, **15**, 401–404.

Anthes, R. A., 1977: A cumulus parameterization scheme utilizing a one-dimensional cloud model. *Mon. Wea. Rev.*, **105**, 270–286.

Atlas, D., S.-H. Chou and W. P. Byerly, 1983: The influence of coastal shape on winter mesoscale air–sea interaction, *Mon. Wea. Rev.*, **111**, 245–252.

Brost, R. A., 1976: Air mass modification in the atmosphere's boundary layers: A study using a two-dimensional numerical model with a higher order turbulence closure. Ph.D. thesis, submitted to the Department of Meteorology, University of Wisconsin, Madison.

Brown, R. A., 1974: *Analytical Methods in Planetary Boundary-Layer Modeling*. Wiley.

Businger, J. A., J. C. Wyngaard, Y. Izumi and E. F. Bradley, 1971: Flux-profile relationships in the atmospheric surface layer. *J. Atmos. Sci.*, **28**, 181–189.

Carlson, T. N., J. K. Dodd, S. G. Benjamin and J. N. Cooper, 1981: Satellite estimation of the surface energy balance, moisture availability and thermal inertia. *J. Appl. Meteor.*, **20**, 67–87.

Chou, S.-H., and D. Atlas, 1982: Satellite estimates of ocean air heat fluxes during cold air outbreak. *Mon. Wea. Rev.*, **110,** 1434–1450.

Cotton, D. E., 1976: Numerical simulation of the orographically induced precipitation distribution for use in hydrostatic analysis. *J. Appl. Meteor.*, **15,** 1241–1252.

Crowley, W. P., 1968: Numerical advection experiments. *Mon. Wea. Rev.*, **96,** 1–11.

Deardorff, J. W., 1978: Efficient prediction of ground surface temperature and moisture, with inclusion of a layer of vegetation. *J. Geophys. Res.*, **83**(C4), 1889–1903.

——, 1980: Stratocumulus-capped mixed layers derived from a three-dimensional model. *Bound.-Layer Meteor.*, **18,** 495–527.

Dirks, R., J. P. Kuettner and J. Moore, 1988: An overview of the Genesis of Atlantic Lows Experiment. *Bull. Amer. Meteor. Soc.*, **69,** 148–160.

Durran, D. R., and J. B. Klemp, 1983: A compressible model for the simulation of moist mountain waves. *Mon. Wea. Rev.*, **111,** 2341–2361.

Hobbs, P. V., 1987: The Gulf Stream rainband. *Geophys. Res. Lett.*, **14,** 1142–1145.

Holt, T., and S. Raman, 1990: Marine boundary layer structure and circulation in the region of offshore redevelopment of a cyclone during GALE. *Mon. Wea. Rev.*, **118,** 392–410.

Huang, C. Y., 1989: A mesoscale planetary boundary layer numerical model for simulations of topographically induced circulations. Ph.D. dissertation, submitted to the Department of Marine, Earth and Atmospheric Sciences, North Carolina State University.

——, and S. Raman, 1988: A numerical modeling study of the marine boundary layer over the Gulf Stream during cold air advection. *Bound.-Layer Meteor.*, **45,** 251–290.

——, and ——, 1989: An application of the E-ϵ closure model to simulations of mesoscale topographic effects. *Bound.-Layer Meteor.*, in press.

Kasten, F., and G. Czeplak, 1980: Solar and terrestrial radiation dependent on the amount and type of cloud. *Sol. Energy*, **24,** 177–189.

Klemp, J. B., and D. K. Lilly, 1978: Numerical simulation of hydrostatic mountain waves. *J. Atmos. Sci.*, **32,** 78–107.

——, and D. R. Durran, 1983: An upper boundary condition permitting internal gravity wave radiation in numerical mesoscale model. *Mon. Wea. Rev.*, **111,** 430–444.

Kuo, H. L., 1965: On formation and intensification of tropical cyclones through latent heat release by cumulus convection. *J. Atmos. Sci.*, **22,** 40–63.

——, 1974: Further studies of the parameterization of the influence of cumulus convection on large-scale flow. *J. Atmos. Sci.*, **31,** 1232–1240.

Leonard, B. P., 1979: A stable and accurate convective modeling procedure based on quadratic upstream interpolation. *Comput. Methods Appl. Mech. Eng.*, **19,** 59–98.

Lin, Y.-L., and R. B. Smith, 1986: Transient dynamics of airflow near a local heat source. *J. Atmos. Sci.*, **43,** 40–49.

Locatelli, J. D., J. M. Sienkiewicz and P. V. Hobbs, 1989: The organization and structure of clouds and precipitation on the mid-Atlantic coast of the United States. Part I: Synoptic evolution of a frontal system from the Rockies to the Atlantic Coast. *J. Atmos. Sci.*, **46,** 1327–1348.

Mahrer, Y., and R. A. Pielke, 1977: The effects of topography on the sea and land breeze in a two-dimensional numerical model. *Mon. Wea. Rev.*, **105,** 1151–1162.

——, and ——, 1978: A test of an upstream spline interpolation technique for the advection terms in a numerical mesoscale model. *Mon. Wea. Rev.*, **106,** 818–830.

McCumber, M. C., and R. A. Pielke, 1981: Simulation of the effects of surface fluxes of heat and moisture in a mesoscale numerical model. 1. Soil layer. *J. Geophys. Res.*, **86,** 9929–9938.

Miller, J. E., 1946: Cyclogenesis in the Atlantic coastal region of the United States. *J. Meteor.*, **3,** 31–44.

Miller, M. J., and A. J. Thorpe, 1981: Radiation conditions for the lateral boundaries of limited area numerical models. *Quart. Roy. Meteor. Soc.*, **107,** 615–628.

Moeng, C.-H., and A. Arakawa, 1980: A numerical study of a marine subtropical stratus cloud layer and its stability. *J. Atmos. Sci.*, **37,** 2661–2676.

Orlanski, I., 1976: A simple boundary condition for unbounded hyperbolic flows. *J. Comput. Phys.*, **21,** 251–269.

Paltrige, G. W., and C. M. R. Platt, 1976: *Radiative Process in Meteorology and Climatology.* Elsevier.

Pielke, R. A., 1984: *Mesoscale Meteorological Modeling.* Academic Press, 612 pp.

Pierrehumbert, R. T., 1984: Linear results on the barrier effects of mesoscale mountains. *J. Atmos. Sci.*, **41,** 1356–1367.

——, and B. Wyman, 1985: Upstream effects of mesoscale mountains. *J. Atmos. Sci.*, **42,** 977–1003.

Raman, S., and A. J. Riordan, 1988: The Genesis of Atlantic Lows Experiment (GALE): The Planetary Boundary Layer Subprogram. *Bull. Amer. Meteor. Soc.*, **69,** 161–172.

Richwein, B. A., 1980: The damming effect of the southern Appalachians. *Nat. Wea. Dig.*, **5,** 2–12.

Sasamori, T., 1972: A linear harmonic analysis of atmospheric motion with radiative dissipation. *J. Meteor. Soc. Japan*, **50,** 505–517.

Shapiro, R., 1971: The use of linear filtering as a parameterization of atmospheric diffusion. *J. Atmos. Sci.*, **28,** 523–531.

Sienkiewicz, J. M., J. D. Locatelli, P. V. Hobbs and B. Geerts, 1989: The organization and structure of clouds and precipitation on the mid-Atlantic coast of the United States. Part II: The mesoscale and microphysical structure of a frontal system. *J. Atmos. Sci.*, **46,** 1349–1364.

Smith, R. B., 1979: The influence of mountains on the atmosphere. *Adv. Geophys.*, **21,** 87–230.

——, and Y.-L. Lin, 1982: The addition of heat to a stratified airstream with application to the dynamics of orographic rain. *Quart. J. Roy. Meteor. Soc.*, **108,** 353–378.

Smolarkiewicz, P. K., R. M. Rasmussen and T. L. Clark, 1988: On the dynamics of Hawaiian cloud bands: Island forcing. *J. Atmos. Sci.*, **45,** 1872–1905.

Sun, W. Y., and W. R. Hsu, 1988: Numerical study of a cold air outbreak over the ocean. *J. Atmos. Sci.*, **45,** 1205–1227.

Wai, M. M.-K., and S. A. Stage, 1989: Dynamical analyses of marine atmospheric boundary layer structure near the Gulf Stream oceanic front. *Quart. J. Roy. Meteor. Soc.*, **115,** 29–44.

Wayland, R., and S. Raman, 1989: Mean and turbulent structure of a baroclinic marine boundary layer during the 28 January 1986 cold-air outbreak (GALE 86). *Bound.-Layer Meteor.*, **48,** 227–254.